FEATURE ARTICLE

Coherent 2D IR Spectroscopy: Molecular Structure and Dynamics in Solution

M. Khalil, N. Demirdöven, and A. Tokmakoff*

Department of Chemistry, Massachusetts Institute of Technology, Cambridge, Massachusetts 02139

Received: August 21, 2002; In Final Form: April 1, 2003

Two-dimensional infrared (2D IR) vibrational spectroscopy is an experimental tool for investigating molecular dynamics in solution on a picosecond time scale. We present experimental and theoretical methods for obtaining a 2D IR correlation spectrum and modeling the underlying microscopic information. Fourier transform 2D spectra are obtained from heterodyne-detected third-order nonlinear signals using a sequence of broad bandwidth femtosecond IR pulses. A 2D IR correlation spectrum with absorptive line shapes results from the addition of 2D rephasing and nonrephasing spectra, which sample conjugate frequencies during the initial evolution time period. The 2D IR spectrum contains peaks with different positions, signs, amplitudes, and line shapes characterizing the vibrational eigenstates of the system and their interactions with the surrounding bath. The positions of the peaks map the transition frequencies between the ground, singly, and doubly excited states of the system and thus describe the anharmonic vibrational potential. Peak amplitudes reflect the relative magnitudes and orientations of the transition dipole moments in the molecular frame, the electrical anharmonicity of the system, and the vibrational relaxation dynamics. The 2D line shapes are sensitive to the system−bath interactions in solution. We illustrate how 2D IR spectra taken with varying polarization conditions and as a function of a variable waiting time can be used to isolate and quantify these spectroscopic observables. As a model vibrational system, we use the strongly coupled asymmetric and symmetric carbonyl stretches of $Rh(CO)_2C_5H_7O_2$ (RDC) dissolved in hexane and chloroform. The polarization-selective 2D IR spectra of RDC in hexane are analyzed in terms of two coupled local coordinates to obtain their mutual orientation and the magnitude of the coupling between them. The 2D line-shape study of RDC in chloroform performed as a function of the waiting period characterizes the system−bath interactions, revealing that the system transition energies fluctuate in a correlated manner.

I. Introduction

The complexity of molecular dynamics in solution lies in understanding the many forces within and between molecules that lead to the time evolution of molecular and collective structures and irreversible relaxation processes. Can we find simplified descriptions of the many covalent and noncovalent interactions present in a complex system to understand conformational changes in solutes, fluctuations in solvent configuration, and vibrational relaxation processes? Furthermore, does understanding the local structure and dynamics arising from short-range intramolecular couplings and solvent interactions allow the behavior of larger systems to be predicted? The answers to such questions are at the heart of predicting the course of chemical reactions and biophysical processes.

Investigations into these phenomena require general experimental methods for describing time-evolving molecular or collective structures. Effective experimental probes of molecular dynamics in solution have to be sensitive to structural changes on picosecond and longer time scales. Also, because transient structures need not be unique, such methods must statistically analyze structural variation within an ensemble and show how this variance evolves with time. One-dimensional (1D) electronic and vibrational spectroscopies have the intrinsic time-resolution required for such studies, but interpreting them is generally ambiguous. When probing a system with many degrees of freedom, 1D spectroscopy projects the ensemble-averaged response of the electronic or nuclear coordinates onto one frequency axis. Analyzing these 1D spectra is an underdetermined problem because they provide a single set of experimental observables that are mutually affected by multiple molecular coordinates. Spectra are often featureless, and it is generally impossible to separate overlapping contributions or line-broadening processes. More importantly, although the signatures of different nuclear or electronic coordinates may be present, the structural and dynamical relationships between these coordinates cannot usually be established.

Multidimensional, nonlinear coherent spectroscopies have been developed to address this problem by disentangling the underlying molecular interactions that are obscured in traditional spectra.[1−3] Such techniques use interactions with a sequence of radiation fields to monitor a system as a function of multiple time periods or frequency variables. Two-dimensional (2D) methods have been used for some time in nuclear magnetic resonance (NMR) as a sensitive tool for determining solution phase structures. In a 2D NMR spectrum, spectral information is spread over two frequency axes, and cross peaks between the resonances on the diagonal axis indicate coupling between

* Corresponding author. E-mail: tokmakof@mit.edu.

10.1021/jp0219247 CCC: $25.00
Published on Web 06/19/2003

spins experiencing different chemical environments.[3,4] Knowledge of the spin-coupling mechanism allows information on connectivity or separation of nuclei to be established. Unfortunately, from a dynamical perspective, 2D NMR has limited use in studying molecular dynamics in solution because the measurement time scale is in the millisecond range.

Two-dimensional infrared (2D IR) spectroscopy is a method that incorporates the structural selectivity of 2D NMR and circumvents the difficulties with traditional IR or optical spectroscopies.[1,5−7] It is one of the several multidimensional optical and IR techniques for the study of molecular structure and dynamics that have been proposed and experimentally realized in the past decade.[1,2,5,7−15] These include 2D Raman experiments,[16−18] 2D electronic correlation spectroscopy,[19−22] and mixed IR−Raman 2D spectroscopies.[23−26] Two-dimensional IR spectroscopy builds on the methodology developed in multidimensional NMR[3,4] and applies it to vibrational resonances whose frequencies are dictated by bonding and local environments. This provides the advantage of probing structurally sensitive resonances with high time resolution. As a probe of time-dependent vibrational energies, couplings, and dipole orientations, it gives information on transient molecular and collective structure, structural variation, solute−solvent interactions, and conformational and vibrational dynamics. Two-dimensional IR spectroscopy can therefore reveal structural changes accompanying time-dependent chemical and biophysical processes in solution.

The focus of this paper is Fourier transform 2D IR spectroscopy. In this third-order nonlinear spectroscopy derived from IR vibrational echoes,[27−30] three femtosecond IR pulses interact with a multilevel vibrational system. The experiment is characterized by three experimental time delays: the evolution (τ_1), waiting (τ_2), and detection (τ_3) periods, which follow the three successive input pulses. In a 2D experiment, the propagation during the evolution and detection periods is observed by varying τ_1 and characterizing the amplitude and phase of a nonlinear signal radiated during τ_3 with a heterodyne detection scheme.[20,21,31,32] The data are represented through a 2D Fourier transform as a 2D spectrum that describes the vibrational transitions sampled during τ_1 and τ_3. Cross peaks reveal couplings and orientations between vibrations and the surrounding bath. The time scale of the experiment ($\tau_1 + \tau_2 + \tau_3$) is typically in the picosecond range, offering a short window to sample the structure and dynamics of the system. Two-dimensional IR spectra collected as a function of τ_2 (a "relaxation experiment") contain signatures of coherent and incoherent vibrational relaxation processes, spectral diffusion phenomena, and fluctuations in vibrational couplings and angles.[22,26,33−36] This information forms the basis for describing structural changes and intermolecular interactions in the condensed phase.

Here we describe our experimental and theoretical efforts in the development of 2D IR spectroscopy for the study of time-evolving molecular structures and relaxation processes in solution. A series of investigations on a rhodium dicarbonyl (RDC) compound are used to present the methods for obtaining intuitive 2D IR spectra and interpreting them to learn about molecular structural dynamics. The amplitudes and positions of the various spectral features in polarization-selective 2D IR spectra of RDC in hexane are used to characterize the anharmonic coupling and the dipole projection angle between the asymmetric and symmetric stretches. This information can be modeled to reveal a transient structure in solution. We show how 2D line shapes studied as a function of the waiting time characterize the interactions of vibrational states with a bath. The changing cross-peak line shapes in 2D IR spectra of RDC in chloroform collected as a function of the waiting period reveal correlated fluctuations of the transition frequencies of the two coupled vibrations. Such information can be modeled to yield details of structural variation, solvation, or conformational fluctuations.

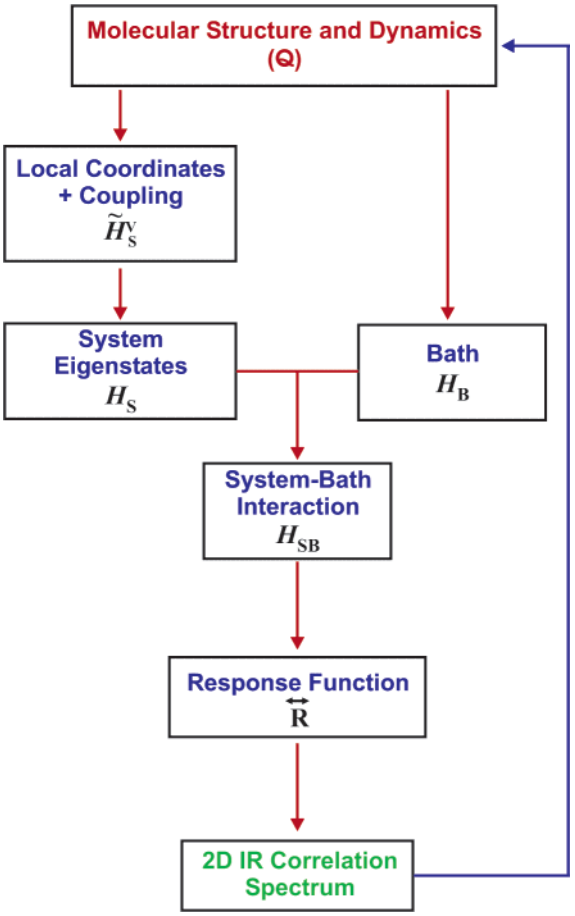

Figure 1. Flowchart describing how we search for an accurate and physically intuitive picture of molecular interactions in solution that reproduce the positions, amplitudes, and line shapes in experimental 2D IR correlation spectra. We start by selecting a complete set of generalized coordinates (**Q**) that yield the most intuitive physical picture. The Hamiltonian $\tilde{H}_S^V(\mathbf{Q})$ describes the couplings between the local coordinates and depends on the local structure(s). Appropriate unitary transformation results in the experimentally measured vibrational eigenstates (H_S). In solution, the system is surrounded by a bath consisting of solvent and/or remaining solute degrees of freedom as described by the bath Hamiltonian (H_B). The effects of the bath on the system are incorporated in the system−bath Hamiltonian (H_{SB}), which is written in the basis of the vibrational eigenstates. The eigenstate parameters are used to calculate the third-order response function ($\overleftrightarrow{\mathbf{R}}$) and to simulate the experimental 2D spectrum. The decoupling of molecular structure from its bath-induced dephasing dynamics results from using a local basis to describe the equilibrium structure and an eigenbasis to describe the effects of the bath on the system.

The flowchart in Figure 1 summarizes our approach toward searching for an accurate and physically intuitive picture of molecular interactions in solution that reproduces the positions, amplitudes, and line shapes in experimental 2D IR correlation spectra. The starting point is a complete set of generalized coordinates that best describe the time-evolving molecular system under study. These coordinates (**Q**) are picked to yield the most intuitive physical picture and can be associated with a specific nuclear coordinate, a normal mode, or a local mode. The properties of the system are contained in the Hamiltonian $\tilde{H}_S^V(\mathbf{Q})$, which describes the couplings between the local coordinates. The coupling parameters reflect the underlying structural

information as dictated by the coupling mechanism. If the system undergoes conformational fluctuations on the time scale of the experiment, then the time dependence of the fluctuations in the couplings between the local coordinates needs to be taken into account. An appropriate unitary (local-to-eigenstate) transformation of the above Hamiltonian results in the vibrational eigenstates whose transition frequencies map onto peak positions in a 2D IR correlation spectrum.

The local-to-eigenstate transformation is intrinsic in most existing analyses of coupled vibrations in 2D IR spectra. The models for one- and two-exciton bands in 2D amide I spectra by Hamm and Hochstrasser[37] and by Mukamel and co-workers[38] use transition-dipole-coupled anharmonic oscillators, and the study of correlated frequency shifts in RDC by Fayer and co-workers used coupled harmonic local oscillators.[29] The nonlinear exciton model has also been used to simulate the 2D IR spectra of small peptides and proteins in which the effects of diagonal and off-diagonal disorder are investigated by allowing for variation in the coupling strength and energies of the local modes.[39] This disorder arises naturally when the site oscillators are chosen to reflect conformational change. The ability of 2D IR spectroscopy to discern different transient structural conformations in the condensed phase is illustrated by recent experiments and molecular dynamics simulations on trialanine[7] and simulations of β-peptide unfolding,[40] which introduce off-diagonal disorder by sampling varying conformations.[41]

In solution, the local coordinates are constantly interacting with a surrounding bath. The properties of the bath, which include the remaining solute and solvent coordinates, are described in the bath Hamiltonian (H_B). The effects of the bath on the system are incorporated in the system−bath Hamiltonian (H_{SB}), which we write in the basis of the vibrational eigenstates. The interaction of the system with the bath can cause fluctuations as well as shifts in the transition energies of the eigenstates. Expressions for the line-shape function are derived from the specific form of H_{SB} and determine the observed amplitude and peak shapes. A 2D IR spectrum can be simulated using the calculated eigenenergies and line-shape functions. Fitting the simulated and experimentally determined spectra reveals the set of local coordinates, their couplings between each other, and the bath modes, which best describe the molecular system under study.

Modeling the 2D line shapes reveals the details of the system−bath interaction (H_{SB}), which contains the effects of the solute−solvent interactions. A description of 2D line shapes using the simple Bloch model shows that homogeneous and inhomogeneous line broadening mechanisms are discerned by the degree of ellipticity of the 2D line shapes.[42,43] Recent theoretical work has largely focused on analyzing 2D line shapes of two-level systems using the Brownian oscillator model of Yan and Mukamel.[44] This model accounts for arbitrary time scales in the description of the system−bath interactions and has been used to model solvation in 2D electronic spectra.[33,45,46] For multilevel vibrational systems, it is necessary to describe the dynamics of multiple transitions.[47] A general approach to this problem that includes all experimental variables has recently been presented by Sung and Silbey. They obtained analytical expressions for the third-order nonlinear response function of a multilevel system coupled to a bath with an arbitrary time scale.[48,49] This is formulated in terms of the auto and cross-correlation functions of the energy-gap fluctuations, which influence the diagonal and cross-peak line shapes in 2D spectroscopy.

The paper is organized as follows. The next section describes our model system of coupled vibrations in detail. In section III, we report on a general theoretical method to calculate 2D correlation spectra, which draws on several existing theories of third-order nonlinear spectroscopy for multilevel systems using polarized light fields. Section IV outlines the procedure for obtaining absorptive line shapes in 2D Fourier transform spectroscopy. The Experimental Section describes the generation and interferometric detection of the signal field, and the following data analysis section shows how the raw data is treated to obtain a 2D correlation spectrum. The analysis of a 2D IR correlation spectrum in terms of the positions, amplitudes, and line shapes of its resonances provides an intuitive description of the system eigenstates and system−bath interactions in section VII. The next sections interpret the experimental 2D spectra in terms of local bond-stretch coordinates and correlated vibrational dynamics of the eigenstates. We end with a discussion of the current results and suggest future directions for this technique.

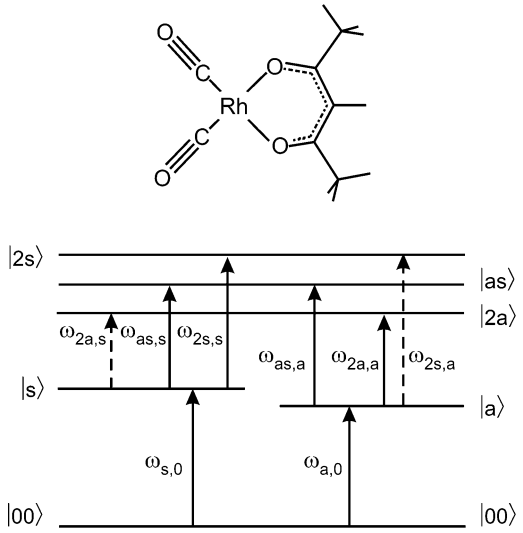

Figure 2. Molecular structure of our model system RDC and the vibrational energy-level diagram for two anharmonically coupled symmetric and asymmetric C≡O vibrations designated as a and s. The six lowest eigenstates are shown as |as⟩, where a and s are the respective vibrational quantum numbers for the asymmetric and symmetric stretches. Solid and dashed arrows indicate the harmonically allowed and harmonically forbidden transitions among the eigenstates, respectively. The actual values of the transition frequencies measured for RDC dissolved in hexane are $\omega_{a,0} = 2015$ cm^{-1}, $\omega_{s,0} = 2084$ cm^{-1}, $\omega_{2a,a} = 2001$ cm^{-1}, $\omega_{2s,s} = 2073$ cm^{-1}, $\omega_{as,a} = 2058$ cm^{-1}, $\omega_{as,s} = 1989$ cm^{-1}, $\omega_{2a,s} = 1932$ cm^{-1}, and $\omega_{2s,a} = 2142$ cm^{-1}.

II. Model System

The generalized multilevel vibrational system probed by third-order IR spectroscopies consists of a set of n fundamental vibrational states and $n(n + 1)/2$ two-quantum states. The transitions into the two-quantum states are combination bands and overtones, whose energy shifts relative to the fundamentals reflect the coupling and anharmonicity of the system. We use the asymmetric and symmetric carbonyl stretches of dicarbonylacetylacetonato rhodium (I) (RDC) dissolved in hexane and chloroform to study the 2D IR spectroscopy of two coupled vibrations. RDC ($Rh(CO)_2C_5H_7O_2$) pictured in Figure 2 is a square-planar d^8 compound with two chemically equivalent terminal carbonyl groups and a bidentate acac ($OC(CH_3)CHC(CH_3)O$) ligand coordinated to the rhodium metal center. The same Figure depicts the six lowest-lying vibrational eigenstates for this particular model system. These six states have been labeled according to the quanta of energy present in the

symmetric and asymmetric stretches. They include a common ground vibrational state (0), the two one-quantum states (a, s), and the three two-quantum states consisting of the overtones (2a, 2s) and the combination band (as).

The fundamental transitions are observed at 2084 (2085) and 2015 (2014) cm^{-1} from the FTIR spectra of RDC dissolved in hexane (chloroform) and are assigned to the symmetric and asymmetric combinations of the $-C\equiv O$ stretches, respectively.[50] The anharmonicity of the nuclear potential, which governs the $-C\equiv O$ stretching motions, leads to the anharmonic frequency shifts of the overtone spectrum. These shifts are measured from the 2D IR correlation spectrum of RDC in hexane at $\Delta_s = 11$ cm^{-1} and $\Delta_a = 14$ cm^{-1} for the symmetric and asymmetric vibrations. The combination band, which reflects the coupling between the carbonyls, is red shifted by $\Delta_{as} = 26$ cm^{-1} with respect to the sum of the fundamental frequencies.

The vibrational dynamics of the carbonyl transitions for RDC in different solvents have been previously characterized with IR pump−probe and two-pulse IR echo spectroscopy.[27,50,51] These studies demonstrated that the narrow line shapes observed for the $-C\equiv O$ stretches of RDC and other metal carbonyls in hexane and 2-methylpentane are well described by the motionally narrowed or homogeneous limit. The full width at half-maximum of the asymmetric and symmetric $-C\equiv O$ stretches of RDC in hexane from the FTIR spectrum (Figure 8) is measured to be ~ 2.6 cm^{-1}, which is significantly narrower than the anharmonic frequency shifts. This allows us to resolve all of the possible resonances in a 2D nonlinear experiment, and we are able to model the structure of RDC on an ~ 20 ps time scale through an analysis of the peak positions and amplitudes of polarization-selective 2D spectra of the molecule dissolved in hexane.[52] The dynamics of the same molecule are completely different in chloroform, where the line widths of the individual asymmetric and symmetric transitions are 14.6 and 9.3 cm^{-1}, respectively, and the anharmonicities remain approximately the same. 2D IR experiments of RDC in chloroform investigate the underlying mechanism of this dramatic change in the 1D absorption line widths and characterize the magnitude and time scales of the correlations in the transition-energy fluctuations of the coupled asymmetric and symmetric vibrational modes.[35]

III. Theoretical Background

Two-dimensional IR correlation spectroscopy belongs to the general class of time-resolved four-wave mixing experiments where three femtosecond IR fields with well-defined wave vectors interact with the sample to generate a nonlinear signal field that contains the microscopic information of interest. This section provides the theoretical background for a semiclassical description of the 2D IR spectroscopy of multilevel vibrational systems. Our purpose is to provide the reader with an approach for simulating polarization-selective 2D IR spectra for a system of coupled vibrations starting from a local or site description of the system of interest and incorporating the influence of the surroundings. We draw on the numerous descriptions of third-order nonlinear spectroscopy present in the literature, but the emphasis here is on the less commonly described response of a multilevel system, for which we follow the treatment of Sung and Silbey.[48,49]

Theoretical descriptions of nonlinear spectroscopy begin with a quantum mechanical material Hamiltonian (H_M) containing information about the system under study and an interaction Hamiltonian (H_{int}) describing the coupling of the system to classical external radiation fields. The total material Hamiltonian is generally written as a sum of the Hamiltonian for the system (H_S), bath (H_B), and the system−bath (H_{SB}) interactions. For the vibrational systems of interest here, H_S contains an arbitrary number of coupled vibrational coordinates **Q**, which are interrogated by the applied radiation. The system Hamiltonian can be expressed in a basis of the local modes,[1,37,52] normal modes,[13,53−57] or eigenstates,[47,48] depending on the information of interest.[7,58−60] Constructing H_S in a local-mode representation allows for an intuitive representation of the molecular structural coordinates of interest. For the purpose of introducing the interaction with a bath, the system eigenstates are coupled to a harmonic bath.[48,61] The system−bath interaction leads to fluctuations and shifts in the vibrational transition frequencies, vibrational relaxation processes, and reorientational dynamics.

The interaction Hamiltonian describing the interaction of the system with the external radiation fields **E** is

$$H_{int} = -\mathbf{M}(\mathbf{Q})\cdot\mathbf{E} = -\sum_{a,b}|a\rangle\boldsymbol{\mu}^{a,b}\cdot\mathbf{E}\langle b| \quad (1)$$

where $\mathbf{M}(\mathbf{Q})$ represents the dipole operator and $\boldsymbol{\mu}^{a,b} = \langle a|\mathbf{M}(\mathbf{Q})|b\rangle$ are the transition dipole matrix elements. Equation 1 expresses the interaction in terms of the system eigenstates (a, b), which are described by a set of vibrational quantum numbers. The dipole operator, expressed as a function of the system vibrational coordinates, can be expanded in a power series around the equilibrium position.[58,62] The linear expansion coefficient $\boldsymbol{\mu}_i^{(1)} = (\partial\mathbf{M}/\partial\mathbf{Q}_i)_{Q_0}$ is the transition dipole moment reflecting the change in the charge distribution through the field-induced displacement of the ith vibrational coordinate. The dipole approximation accounts for only the linear term in the above expansion, leading to the selection rule for linear IR spectroscopy of $\Delta n = \pm 1$ for the vibrational quantum number n. The nonlinear dependence of the dipole operator on the vibrational coordinates, or electrical anharmonicity, is indicated by the presence of nonzero values of higher-order expansion coefficients $\boldsymbol{\mu}^{(n)}$, which relax the above-mentioned selection rule and affect the intensity ratios of fundamentals to their corresponding overtone bands.

The electric field **E** in eq 1 is a real quantity expressed as a linearly polarized plane wave

$$\mathbf{E}(\mathbf{k}, \nu, t) = \sum_J \hat{J}\,\epsilon_J(t)\cos(2\pi\nu t + \varphi(t) - \mathbf{k}\cdot\mathbf{r}) \quad (2)$$

where **k** is the incident wave vector, ν is the carrier frequency, $\varphi(t)$ is the time-dependent phase, and $\epsilon(t)$ is the time-dependent electric-field envelope. The polarization direction of the electric-field vector is given by the unit vector $\hat{J}$ expressed in the Cartesian coordinates of the laboratory fixed frame $\hat{J} \in \{X, Y, Z\}$.

Two-dimensional IR spectroscopy measures the third-order nonlinear polarization $\mathbf{P}^{(3)}$ induced by the interaction of the material with three IR fields. The formal expression for $\mathbf{P}^{(3)}$ written in the interaction picture after a perturbative expansion of the interaction Hamiltonian is given by

$$\mathbf{P}^{(3)}(\mathbf{k}_s, t, \tau_2, \tau_1) = \int_0^\infty\int_0^\infty\int_0^\infty \vec{\mathbf{R}}(\tau_3', \tau_2', \tau_1')\vdots\mathbf{E}_3(\mathbf{k}_3, \nu_3, t-\tau_3')\times \mathbf{E}_2(\mathbf{k}_2, \nu_2, t+\tau_2-\tau_3'-\tau_2')\times \mathbf{E}_1(\mathbf{k}_1, \nu_1, t+\tau_2+\tau_1-\tau_3'-\tau_2'-\tau_1')\,d\tau_1'\,d\tau_2'\,d\tau_3' \quad (3)$$

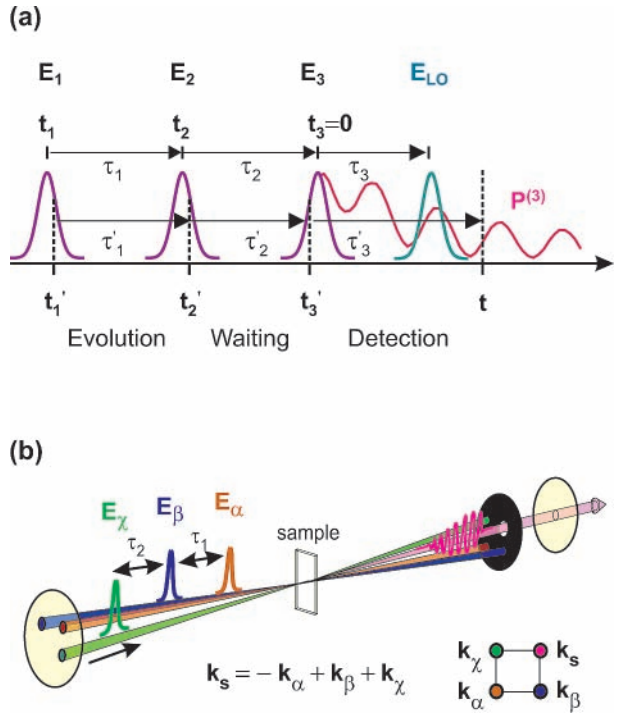

Figure 3. (a) Pulse sequence and time variables for a 2D IR experiment. The field−matter interactions occur at times t'_n within the envelope of the three input pulses $\mathbf{E}_n$ to radiate a third-order nonlinear polarization, $\mathbf{P}^{(3)}$ at time t following the final pulse. The variables τ_n represent the experimentally controlled delays between successive input fields measured with respect to the center of the pulses, t_n. The variables τ'_n represent the time interval between the field−matter interactions, $(t_{n+1} - t_n)$. The amplitude and phase of the signal field radiated from the sample is obtained by mixing it with a well-characterized local oscillator ($\mathbf{E}_{LO}$) field, which is delayed by τ_3 with respect to the final input pulse. The experimental delays τ_1, τ_2, and τ_3 are known as the evolution, waiting, and detection periods, respectively. (b) Noncollinear "boxcars" phase-matching geometry for the three input fields in 2D IR spectroscopy. The top panel shows the three beams $\mathbf{E}_\alpha$, $\mathbf{E}_\beta$, and $\mathbf{E}_\chi$ entering the sample in boxcar geometry and the signal being emitted in the phase-matched direction: $\mathbf{k}_s = -\mathbf{k}_\alpha + \mathbf{k}_\beta + \mathbf{k}_\chi$.

$\vec{\mathbf{R}}(\tau'_3, \tau'_2, \tau'_1)$ is the material response function, and the various time variables in eq 3 are illustrated in Figure 3a. The maximum of the field envelopes representing their relative positions are denoted by t_n, and the times at which the successive field−matter interactions occur within the field envelope are represented by t'_n. The delays between the successive input pulses and the successive field−matter interactions are given by $\tau_n = t_{n+1} - t_n$ and $\tau'_n = t'_{n+1} - t'_n$, respectively. The experimental delays τ_1, τ_2, and τ_3 are known as the evolution, waiting, and detection time periods, respectively.

The material response for a third-order resonant experiment is expressed as a four-point correlation function of the dipole operator and contains information about the time evolution under the material Hamiltonian,[63]

$$\vec{\mathbf{R}}(\tau'_3, \tau'_2, \tau'_1) = \left(\frac{i}{\hbar}\right)^3 \langle [[[\mathbf{M}(\tau'_3 + \tau'_2 + \tau'_1), \mathbf{M}(\tau'_2 + \tau'_1)], \mathbf{M}(\tau'_1)], \mathbf{M}(0)]\boldsymbol{\rho}_0 \rangle \quad (4)$$

Here $\boldsymbol{\rho}_0$ is the equilibrium reduced density matrix for the system eigenstates. The commutator in eq 4 can be expanded into eight terms:[61]

$$\vec{\mathbf{R}}(\tau'_3, \tau'_2, \tau'_1) = \sum_{n=1}^{4} \vec{\mathbf{R}}_n(\tau'_3, \tau'_2, \tau'_1) - \vec{\mathbf{R}}^*_n(\tau'_3, \tau'_2, \tau'_1) \quad (5)$$

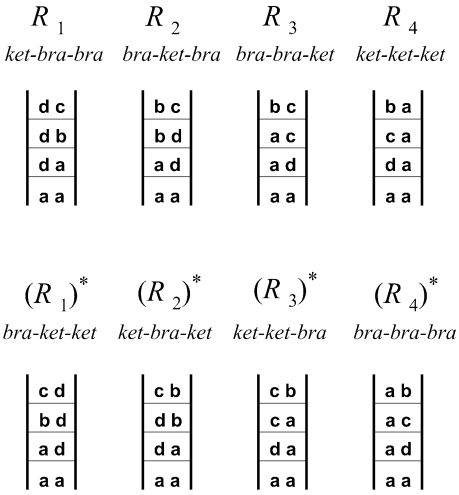

Figure 4. Evolution of the density matrix for each of the eight terms resulting from the expansion of the total resonant third-order material response function given in eq 4. The indices *abcd* represent the eigenstates of the system under study.

These represent the set of Liouville pathways pictured in Figure 4 describing the evolution of the system during τ'_1, τ'_2, and τ'_3 following interaction with the light fields at t'_1, t'_2, and t'_3. The response function is a fourth-rank tensor quantity that contains not only the information relevant to vibrational dynamics but also the relative orientation and orientational dynamics of the dipoles interrogated by the polarized electric fields. Most descriptions of the nonlinear response assume an isotropic material Hamiltonian. This assumption is of limited use for multilevel vibrational systems where the relative orientations of coupled transition dipoles will affect the material response function probed by polarized light fields.[64−66]

Tensorial descriptions of the nonlinear response generally begin with the simplifying assumption that the vibronic and rotational degrees of freedom are separable.[61,64,67] This separation of variables also allows the transition moments to be written as a product of a unit vector $\hat{\boldsymbol{\mu}}^{a,b}$ along the coordinate(s) that couples eigenstates a and b and the magnitude $\mu^{a,b}$ of the transition dipole matrix element

$$\boldsymbol{\mu}^{a,b} = \hat{\boldsymbol{\mu}}^{a,b}\mu^{a,b} \quad (6)$$

Following this argument, each of the tensorial responses in eq 5 can be written as a product of an isotropic nonlinear vibrational response function $R_n^{a,b,c,d}$, which describes the vibrational dynamics, and a tensorial nonlinear orientational response function $(Y_n)_{IJKL}^{a,b,c,d}$, which describes the influence of dipole orientation and orientational dynamics:[64]

$$\vec{\mathbf{R}}_n(\tau'_3, \tau'_2, \tau'_1) = \sum_{IJKL} \sum_{a,b,c,d} (Y_n)_{IJKL}^{a,b,c,d}(\tau'_3, \tau'_2, \tau'_1)\, R_n^{a,b,c,d}(\tau'_3, \tau'_2, \tau'_1) \quad (7)$$

The indices for the orientational response (I, J, K, L) refer to a permutation over the laboratory frame indices $\{X, Y, Z\}$. The evaluation of the sum over orientational indices in eq 7 is greatly simplified when considering the symmetry relationships for isotropic media, which result in four nonvanishing tensor components Y_{ZZZZ}, Y_{ZZYY}, Y_{ZYZY}, and Y_{ZYYZ}, three of which are independent: $Y_{ZZZZ} = Y_{ZZYY} + Y_{ZYZY} + Y_{ZYYZ}$.[68]

Nonlinear Vibrational Response. Using the Liouville pathways illustrated in Figure 4, we can write the four vibrational response functions as[48]

$$R_1^{a,b,c,d}(\tau_3', \tau_2', \tau_1') = P_a \mu^{c,d}\mu^{b,c}\mu^{a,b}\mu^{d,a} \exp(-i\omega_{d,c}^0\tau_3' - i\omega_{d,b}^0\tau_2' - i\omega_{d,a}^0\tau_1')F_1^{a,b,c,d}(\tau_3', \tau_2', \tau_1') \quad (8a)$$

$$R_2^{a,b,c,d}(\tau_3', \tau_2', \tau_1') = P_a \mu^{c,b}\mu^{d,c}\mu^{b,a}\mu^{a,d} \exp(-i\omega_{b,c}^0\tau_3' + i\omega_{d,b}^0\tau_2' + i\omega_{d,a}^0\tau_1')F_2^{a,b,c,d}(\tau_3', \tau_2', \tau_1') \quad (8b)$$

$$R_3^{a,b,c,d}(\tau_3', \tau_2', \tau_1') = P_a \mu^{c,b}\mu^{b,a}\mu^{d,c}\mu^{a,d} \exp(-i\omega_{b,c}^0\tau_3' + i\omega_{c,a}^0\tau_2' + i\omega_{d,a}^0\tau_1')F_3^{a,b,c,d}(\tau_3', \tau_2', \tau_1') \quad (8c)$$

$$R_4^{a,b,c,d}(\tau_3', \tau_2', \tau_1') = P_a \mu^{a,b}\mu^{b,c}\mu^{c,d}\mu^{d,a} \exp(-i\omega_{ba}^0\tau_3' - i\omega_{ca}^0\tau_2' - i\omega_{da}^0\tau_1')F_4^{a,b,c,d}(\tau_3', \tau_2', \tau_1') \quad (8d)$$

In the above equations, P_a reflects the probability of occupying the initial state a. Equation 8 shows that the nonlinear vibrational response function is a product of the magnitudes of the four interacting dipoles ($\mu^{p,q}$), an exponential oscillating at the system eigenfrequencies ($\omega_{p,q}^0 = (E_p^0 - E_q^0)/\hbar$) sampled during τ_1', τ_2', and τ_3', and a nonlinear dephasing function ($F_n^{a,b,c,d}$).

Analytical solutions for the dephasing functions are obtained by approximating the system−bath interaction Hamiltonian as diagonal in the system eigenstates, which describes transition-energy fluctuations induced by the system−bath interactions. The time-dependent fluctuations of the vibrational transition frequency $\omega_{p,q}$ can be expressed as the bath-induced frequency shifts $\delta\omega_{p,q}$ about the ensemble-averaged value $\omega_{p,q}^0$:

$$\omega_{p,q}(t) = \omega_{p,q}^0 + \delta\omega_{p,q}(t) \quad (9)$$

The time scales of these fluctuations for the different vibrational transitions are expressed in terms of the energy gap auto (ζ_{pp}) and cross- (ζ_{pq}) correlation functions[48]

$$\zeta_{pq}(t) = \langle \delta\omega_{p,a}(t)\, \delta\omega_{q,a}(0)\rangle \quad (10)$$

ζ correlates the fluctuations in the $\omega_{q,a}$ transition-energy gap with the $\omega_{p,a}$ energy gap over a time period t, where a is the initial state of the density matrix. Formulating the nonlinear dephasing functions in terms of both auto- and cross-correlation functions demonstrates that 2D vibrational spectroscopies are sensitive to the correlations between the energy-gap fluctuations of different vibrational coordinates.[13,47,69] We include the effects of population relaxation with a phenomenological exponential damping constant. The above approximation works well for molecular systems where the dominant relaxation processes are bath-induced vibrational dephasing and reorientational dynamics, such as the metal carbonyls studied here.[70−72]

In this formalism, arbitrary time scales can be used to describe the system−bath interactions. Often it is adequate or simpler to model experimental data in the limits of extremely fast (homogeneous) or extremely slow (inhomogeneous) time scales for the system−bath interactions. The explicit expressions for the nonlinear dephasing functions in the two limiting cases are given in the Supporting Information.[73] For a multilevel vibrational system, the nonlinear dephasing function is expressed in terms of energy-gap correlation functions involving the ground, singly, and doubly excited vibrational states.[74−78] In the case of weakly anharmonic systems, this large set of correlation functions can be reduced by using the harmonic approximation to express the frequency fluctuations between the one- and two-quantum states in terms of the frequency fluctuations between the ground and one-quantum states, as described in the Supporting Information.

Nonlinear Orientational Response. We now turn our attention to the calculation of the orientational response function, which has been described in detail in refs 64 and 48 within the model of orientational diffusion. This response reflects the sequential projection of the electric fields in the laboratory frame onto the molecular transition dipole moments for a particular sequence of electric-field interactions, allowing the rigid molecules to diffuse orientationally between successive field−matter interactions. Starting from an isotropic distribution, each field interaction projects out a subset of molecules from the evolving orientational distribution. The orientational response is evaluated by (1) expressing the orientation of the four time-ordered transition dipole operators in a molecular body-fixed frame ($i, j, k, l \in x, y, z$) and (2) transforming the motion in the molecular frame into the laboratory frame through an orientational average. The four factors Y_n differ only in the sequence of interactions with the electric field:

$$(Y_1)_{IJKL}^{a,b,c,d}(\tau_3', \tau_2', \tau_1') = \sum_{ijkl} \tilde{Y}_{IJKL}^{ijkl}(\tau_3', \tau_2', \tau_1')[\hat{\boldsymbol{\mu}}^{c,d}\cdot\hat{i}][\hat{\boldsymbol{\mu}}^{b,c}\cdot\hat{j}][\hat{\boldsymbol{\mu}}^{a,b}\cdot\hat{k}][\hat{\boldsymbol{\mu}}^{d,a}\cdot\hat{l}] \quad (11a)$$

$$(Y_2)_{IJKL}^{a,b,c,d}(\tau_3', \tau_2', \tau_1') = \sum_{ijkl} \tilde{Y}_{IJKL}^{ijkl}(\tau_3', \tau_2', \tau_1')[\hat{\boldsymbol{\mu}}^{c,b}\cdot\hat{i}][\hat{\boldsymbol{\mu}}^{d,c}\cdot\hat{j}][\hat{\boldsymbol{\mu}}^{b,a}\cdot\hat{k}][\hat{\boldsymbol{\mu}}^{a,d}\cdot\hat{l}] \quad (11b)$$

$$(Y_3)_{IJKL}^{a,b,c,d}(\tau_3', \tau_2', \tau_1') = \sum_{ijkl} \tilde{Y}_{IJKL}^{ijkl}(\tau_3', \tau_2', \tau_1')[\hat{\boldsymbol{\mu}}^{c,b}\cdot\hat{i}][\hat{\boldsymbol{\mu}}^{b,a}\cdot\hat{j}][\hat{\boldsymbol{\mu}}^{d,c}\cdot\hat{k}][\hat{\boldsymbol{\mu}}^{a,d}\cdot\hat{l}] \quad (11c)$$

$$(Y_4)_{IJKL}^{a,b,c,d}(\tau_3', \tau_2', \tau_1') = \sum_{ijkl} \tilde{Y}_{IJKL}^{ijkl}(\tau_3', \tau_2', \tau_1')[\hat{\boldsymbol{\mu}}^{a,b}\cdot\hat{i}][\hat{\boldsymbol{\mu}}^{b,c}\cdot\hat{j}][\hat{\boldsymbol{\mu}}^{c,d}\cdot\hat{k}][\hat{\boldsymbol{\mu}}^{d,a}\cdot\hat{l}] \quad (11d)$$

The transformation of the diffusive orientational motion of the molecular frame into the laboratory frame is treated classically and is expressed as a four-point joint probability function:

$$\tilde{Y}_{IJKL}^{ijkl}(\tau_3', \tau_2', \tau_1') = \int d\Omega_3 \int d\Omega_2 \int d\Omega_1 \int d\Omega_0 [\hat{i}(\Omega_3)\cdot\hat{I}] \times G(\Omega_3, \tau_3'|\Omega_2)[\hat{j}(\Omega_2)\cdot\hat{J}]G(\Omega_2, \tau_2'|\Omega_1)[\hat{k}(\Omega_1)\cdot\hat{K}] \times G(\Omega_1, \tau_1'|\Omega_0)[\hat{l}(\Omega_0)\cdot\hat{L}]P(\Omega_0) \quad (12)$$

In the above expression, Ω represents the Euler angles that transform the microscopic frame into the laboratory fixed frame, and $P(\Omega_0) = 1/8\pi^2$ is the initial isotropic orientation of the molecules. Note that the time ordering of the polarization indices are read from right to left. The term $G(\Omega_{n+1}, \tau_{n+1}'|\Omega_n)$ is a conditional probability that relates the initial orientation of a molecule Ω_n to an orientation Ω_{n+1} after a time τ_{n+1}' assuming that $\Omega(t)$ is a Markovian process on the experimental time scale. These conditional probability functions have been described for solutions to various orientational diffusion equations.[79,80] The analytical expressions for $\tilde{Y}_{IJKL}^{ijkl}$ are tabulated, and the calculation of the diffusive orientational response is further described in the Supporting Information. In practice, the summation over microscopic frame indices in eq 11 is greatly simplified by using the existing symmetry relations regarding the interchange of the laboratory and microscopic frame indices.[64] A judicious choice of polarizations for the incident fields or a combination of experiments with varying polarization can be used to reveal the relative orientation of the system transition dipole moments and to separate the contributions of the vibrational and orientational responses in the measured signal.[52,81,82]

Phase Matching and Pulse Time-Ordering. For the resonant 2D IR experiments described in this paper, we consider three input fields $\mathbf{E}_\alpha$, $\mathbf{E}_\beta$, and $\mathbf{E}_\chi$, each with a unique incident wavevector $\mathbf{k}_\alpha$, $\mathbf{k}_\beta$, or $\mathbf{k}_\chi$, respectively. The polarization vectors of the input fields α, β, and χ are represented by the indices *L*, *K*, and *J*, respectively. These pulses cross in the sample to generate a third-order nonlinear polarization, which radiates a signal field in the $\mathbf{k}_s = -\mathbf{k}_\alpha + \mathbf{k}_\beta + \mathbf{k}_\chi$ phase-matched direction (Figure 3b). For this phase-matching condition and assuming the rotating wave approximation, there are 16 double-sided Feynman diagrams relevant to a multilevel vibrational system derived from the eight Liouville pathways shown in Figure 4. These 16 diagrams, illustrated in Figure 5, describe the evolution of the density matrix for all of the possible time orderings (1−2−3) of the wavevectors α, β, and χ. Each diagram, in turn, has a number of components depending on the specific Liouville pathway for the six eigenstates of our system: the ground state 0, the one-quantum states $1 \in \{a, s\}$, and the two-quantum states $2 \in \{2a, as, 2s\}$. The diagrams are broadly separated into two main categories of rephasing (S_I) and nonrephasing (S_{II} and S_{III}) third-order response functions. They are further classified by the time orderings of pulses along the incident wavevectors as $S_I = -\mathbf{k}_1 + \mathbf{k}_2 + \mathbf{k}_3$, $S_{II} = +\mathbf{k}_1 - \mathbf{k}_2 + \mathbf{k}_3$, and $S_{III} = +\mathbf{k}_1 + \mathbf{k}_2 - \mathbf{k}_3$.[83] In a rephasing (or echo) experiment, the phase acquired by coherences during the evolution period, $e^{i\omega_{pa}\tau'_1}$, is the conjugate of that for the detection period $e^{-i\omega_{pa}\tau'_3}$.[84] The nonrephasing diagrams of S_{II} and S_{III} evolve with the same frequency during τ'_1 and τ'_3 and cannot rephase macroscopically. Note that the contributions from S_{III} are unique to multilevel systems, where it is possible to create a vibrational coherence between the ground state and the two-quantum state after the first two interactions.

For the purposes of simulating the experimental signals, we assume that the pulse length in our experiment is much shorter than any of the vibrational dynamics of interest, making the evaluation of the triple convolution integral in eq 3 trivial. In this limit, we take the observed time-domain signal to be

$$\mathbf{S}(\mathbf{k}_s, \tau_3, \tau_2, \tau_1) \propto Re[\vec{\mathbf{R}}(\tau_3, \tau_2, \tau_1)] \qquad (13)$$

The data are represented as a correlation map of frequencies through a double Fourier transform

$$\tilde{\mathbf{S}}(\mathbf{k}_s, \omega_3, \tau_2, \omega_1) = \mathbf{Re}\left[\int_{-\infty}^{\infty}\int_{-\infty}^{\infty} S(\mathbf{k}_s, \tau_3, \tau_2, \tau_1)\, e^{i\omega_1\tau_1}\, e^{i\omega_3\tau_3}\, d\tau_1\, d\tau_3\right] \qquad (14)$$

where ω_1 and ω_3 are Fourier transform pairs of the experimental delays, τ_1 and τ_3.

IV. Absorptive Line Shapes in 2D FT Spectroscopy

Information about the material response is contained in the positions, amplitudes, and line shapes of the resonances in a 2D correlation spectrum. For well-separated resonances, an absolute value 2D spectrum is sufficient to reveal the spectroscopic observables necessary to obtain information about molecular structure and dynamics. In congested absolute value 2D spectra, the broad wings and missing sign of the resonances hinder the analysis. Even the real value 2D Fourier transform spectrum of a particular phase-matched signal (i.e., rephasing or nonrephasing) is not ideal because it contains "phase-twisted" peaks, with inherently mixed absorptive and dispersive character. For an intuitive interpretation and simplified modeling of 2D spectra, purely absorptive features free of distorting dispersive components are desired.

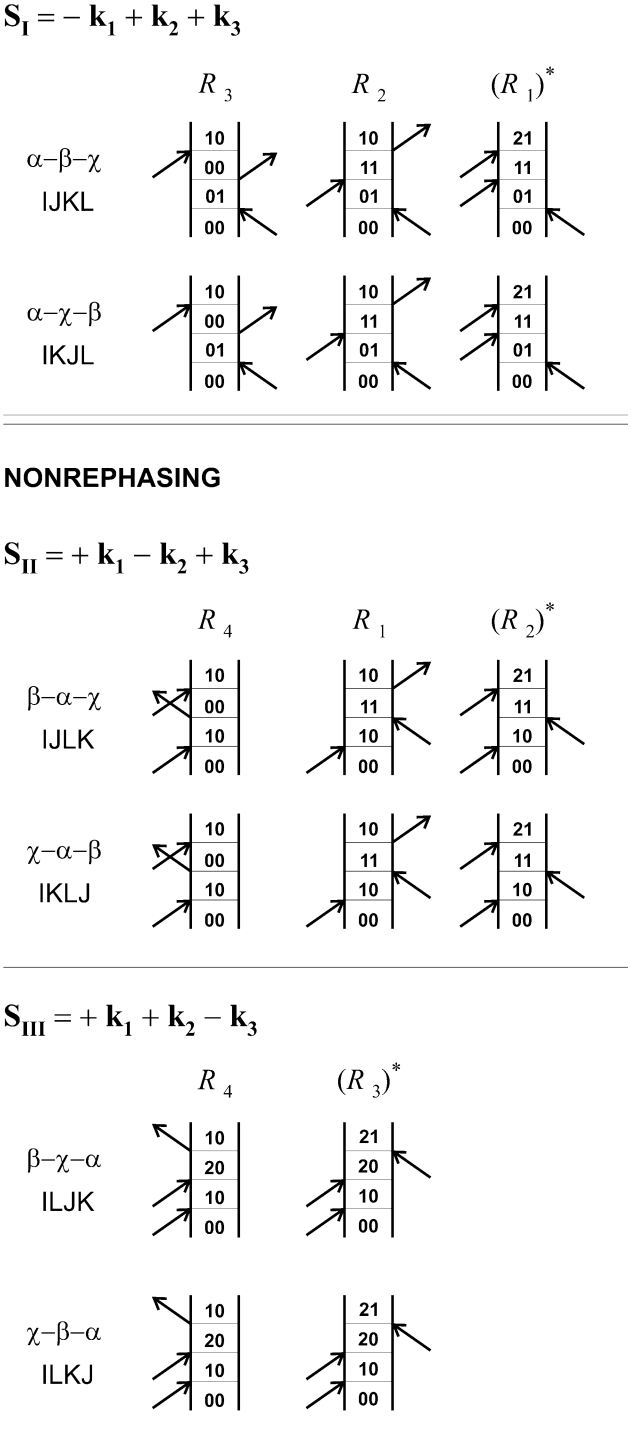

Figure 5. Double-sided Feynman diagrams contributing to the rephasing and nonrephasing Liouville-space pathways for all possible time ordering of the input fields $\mathbf{E}_\alpha$, $\mathbf{E}_\beta$, and $\mathbf{E}_\chi$ given the phase-matching condition $\mathbf{k}_s = -\mathbf{k}_\alpha + \mathbf{k}_\beta + \mathbf{k}_\chi$. The numberings 0, 1, and 2 represent the ground, first, and second excited states of a multilevel system. For our model system RDC, $1,1' \in \{a, s\}$ and $2 \in \{2a, as, 2s\}$. Note that the polarization indices (*I, J, K, L*) are read from right to left.

As observed originally in 2D NMR, the line shapes obtained from any 2D FT spectroscopy are of a mixed-phase character.[3] Absorptive line shapes in 2D spin correlation spectra are obtained by phase-cycling techniques where two signals oscillating with conjugate frequencies during the evolution period are added to remove the dispersive character of the phase-twisted

peaks.[85,86] In the case of nonlinear optical and IR spectroscopy, the use of a noncollinear excitation geometry where the signal is heterodyne-detected in a specific phase-matched direction substitutes for phase cycling used in NMR.[21,33,61,83,87] The phase relationship between the vibrational frequencies excited during the initial and final time periods is dictated by the time ordering of the input pulses for a particular phase-matching geometry. A 2D IR correlation spectrum with absorptive line shapes is obtained by the summation of 2D spectra measured by complementary rephasing and nonrephasing experiments.[32] These experiments sampling conjugate frequencies in the initial time period are performed in a fixed phase-matched direction by exchanging the sequence of the first two pulses along the incident wavevectors.

The time sequences for the three input pulses (1−2−3) entering the sample for the rephasing and nonrephasing experiments are $\alpha - \beta - \chi$ and $\beta - \alpha - \chi$. When $\tau_2 = 0$ and the last two pulses are time-coincident on the sample, the pulse orderings for the rephasing sequence $\alpha - \beta - \chi$ and $\alpha - \chi - \beta$ are indistinguishable. Similarly, contributions from the pulse orderings $\beta - \alpha - \chi$ and $\beta - \chi - \alpha$ are present in the nonrephasing experiment when $\tau_2 = 0$. The Liouville pathways sampled by the rephasing experiments at $\tau_2 = 0$ are illustrated in the first two rows of Figure 5, and those sampled in the nonrephasing experiment are shown in the fourth and sixth row of the same Figure. The presence of the S_{III} contribution at $\tau_2 = 0$ in the nonrephasing response for multilevel systems avoids the discontinuity at $\tau_1 = 0$ that has been predicted and observed for two-level systems in 2D electronic spectroscopy.[33,88]

Figure 6 offers a pictorial representation of how the sum of 2D spectra obtained from conjugate rephasing and nonrephasing experiments gives rise to absorptive features. The response functions R_R and R_{NR} for rephasing and nonrephasing experiments on a two-level system are illustrated in Figure 6a, showing that the system evolves in conjugate frequencies during the evolution period. The signal for each of these experiments, written using the procedure outlined in section III for infinitely short input pulses, is

$$\mathbf{S}_R(\mathbf{k}_s, \tau_3, \tau_2, \tau_1) \propto (Y_2)^{0,a,0,a}_{ZZZZ}\, \mu^{0,a}\mu^{a,0}\mu^{a,0}\mu^{0,a} \times \exp(-i\omega^0_{a,0}\tau_3 + i\omega^0_{a,0}\tau_1)\, F_2^{0,a,0,a}(\tau_3, \tau_2, \tau_1) + c.c. \quad (15)$$

$$\mathbf{S}_{NR}(\mathbf{k}_s, \tau_3, \tau_2, \tau_1) \propto (Y_1)^{0,a,0,a}_{ZZZZ}\, \mu^{0,a}\mu^{a,0}\mu^{a,0}\mu^{0,a} \times \exp(-i\omega^0_{a,0}\tau_3 - i\omega^0_{a,0}\tau_1)\, F_1^{0,a,0,a}(\tau_3, \tau_2, \tau_1) + c.c. \quad (16)$$

In the above expression, the polarization of the input fields is aligned along the $\hat{\mathbf{Z}}$ axis in the laboratory fixed frame. We assume that the dynamics of the system can be described in the motionally narrowed limit, for which $F_2^{0,a,0,a} = F_1^{0,a,0,a} = \exp[-(\Gamma_{aa}\tau_3 + \Gamma_{aa}\tau_1)]$ at $\tau_2 = 0$. The time scale of the system−bath interactions resulting in the fluctuations of the transition energies of state a with respect to the ground state 0 is given by Γ^{-1}_{aa}. The only difference in the two signals $\mathbf{S}_R$ and $\mathbf{S}_{NR}$ is the oscillation of the system in conjugate frequencies during the evolution period. The 2D spectra are obtained after a double Fourier transform of the response functions following eq 14 and setting $\tau_2 = 0$ in the above equations.

The rephasing and nonrephasing 2D spectra are plotted below their respective response functions in Figure 6b. We see that the spectral representation of the rephasing and nonrephasing signals $\tilde{\mathbf{S}}'_R$ and $\tilde{\mathbf{S}}_{NR}$ appear in the $(\mp\omega_1, \pm\omega_3)$ and $(\pm\omega_1, \pm\omega_3)$ quadrants of the Fourier plane, respectively. The conjugate symmetry for $\tilde{\mathbf{S}}'_R$ and $\tilde{\mathbf{S}}_{NR}$ results from the oscillation of the system in conjugate frequencies during τ_1 for the two experiments. Figure 6c shows the mirror image of the rephasing spectrum in the $(\pm\omega_1, \pm\omega_3)$ quadrants. We will refer to this mirror image as the rephasing spectrum $\tilde{\mathbf{S}}_R$ in the rest of the paper, and it will be plotted in the (ω_1, ω_3) quadrant of the Fourier plane.

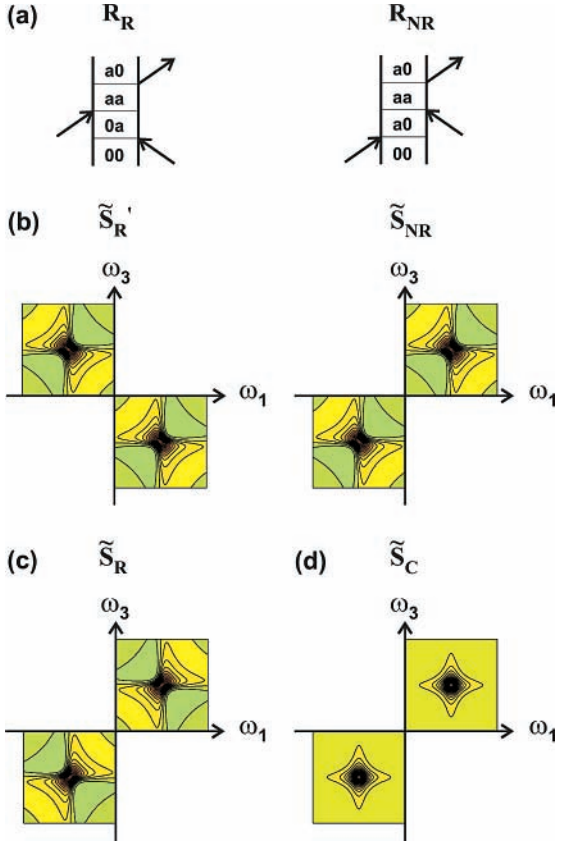

Figure 6. (a) Feynman diagrams for a particular rephasing and nonrephasing pathway for a two-level system consisting of a ground (0) and an excited state. (b) Corresponding 2D spectra ($\tilde{\mathbf{S}}'_R$ and $\tilde{\mathbf{S}}_{NR}$) showing phase-twisted features plotted in the $(\mp\omega_1, \pm\omega_3)$ and $(\pm\omega_1, \pm\omega_3)$ quadrants of the Fourier plane, respectively. (c) Mirror image ($\tilde{\mathbf{S}}_R$) of the 2D rephasing spectrum plotted in the $(\pm\omega_1, \pm\omega_3)$ quadrants. (d) Purely absorptive 2D correlation spectrum obtained from the addition of the nonrephasing ($\tilde{\mathbf{S}}_{NR}$) and rephasing ($\tilde{\mathbf{S}}_R$) 2D spectra in b and c.

The rephasing and nonrephasing 2D spectra plotted in the (ω_1, ω_3) quadrant show phase-twisted line shapes elongated along the diagonal and off-diagonal axes. This phase-twisted line shape is composed of absorptive and dispersive features.[3,89] Only a slice taken exactly along the resonance in either frequency dimension yields an absorptive feature. The line shape becomes distorted for a slice taken slightly off-resonance along any frequency dimension. The addition of the two spectra, shown in Figure 6d, yields a purely absorptive feature by canceling the dispersive components of the individual spectra.

The purely absorptive line shape shown in Figure 6d results from the addition of equally weighted rephasing and nonrephasing Liouville pathways. Figure 7 illustrates line shapes obtained in 2D IR correlation spectra from the summation of unequally weighted rephasing and nonrephasing pathways. These 2D line shapes have some mixed-phase character reflected by their varying tilts from the ω_1 axis. The degree of phase twist can be quantified by an angle Ψ given by $\tan(\Psi) = (A_R - A_{NR})/(A_R + A_{NR})$, where A_R and A_{NR} represent the amplitudes of the

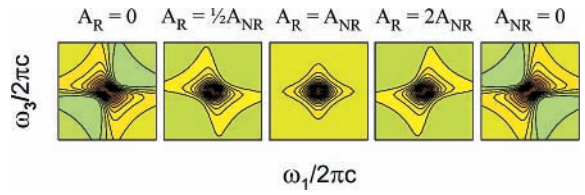

Figure 7. Phase-twisted line shapes in 2D correlation spectra resulting from the addition of unequally weighted rephasing and nonrephasing signals. A_R and A_{NR} represent the amplitudes of the rephasing and nonrephasing signals, respectively. For the five cases illustrated, $A_R = 0$, $A_R = (1/2)A_{NR}$, $A_R = A_{NR}$, $A_R = 2A_{NR}$, and $A_{NR} = 0$, the phase-twist angle $\Psi = 3\pi/4$, $3\pi/5$, 0, $\pi/10$, and $\pi/4$.

rephasing and nonrephasing signals, respectively.[3] The above definition implies that when $A_{NR} < A_R$ the 2D line shape will be tilted along the diagonal axis and $0 < \Psi < \pi/4$. Alternatively, the line shape will be tilted along the off-diagonal axis when $A_R < A_{NR}$ and $\pi/2 < \Psi < 3\pi/4$.[32]

There are a number of effects that give rise to differing amplitudes in the rephasing and nonrephasing signals for a particular peak in a 2D IR correlation spectrum. The first is an unequal sampling of rephasing and nonrephasing pathways to form the same spectral feature in the 2D correlation spectrum.[33] For all multilevel vibrational systems, there exists an inherent asymmetry in the number of rephasing and rephasing pathways contributing to the formation of some of the features in a 2D correlation spectrum. This results in the cross peaks being tilted with respect to the diagonal peaks in the 2D IR correlation spectrum of RDC in hexane.[32] Other than a discrepancy in the number of pathways, the relative amplitudes of the rephasing and nonrephasing signals are also affected by microscopic factors contained in the material response of the system probed during the two different experiments. These factors include the effects of dephasing dynamics sampled differently by the rephasing and nonrephasing experiments.[46,69] With respect to signals $\mathbf{S}_R$ and $\mathbf{S}_{NR}$ given in eqs 15 and 16, this would imply that the two nonlinear dephasing functions are different and as a result $F_2^{0,a,0,a} \neq F_1^{0,a,0,a}$. The effects of inhomogeneity present in the system and the degree of correlation of inhomogeneity between coupled modes are observed experimentally in the 2D IR correlation spectrum of RDC in chloroform.[325] Different orientational contributions Y_{IJKL}^{ijkl} to the rephasing and nonrephasing spectrum also result in phase-twisted line shapes as seen in the polarization-selective 2D IR correlation spectra of RDC dissolved in hexane.

V. Experimental Section

Coherent 2D IR experiments on multilevel vibrational systems are performed using short pulses with enough spectral bandwidth to excite all of the vibrational transitions of interest. The experimental technique to obtain 2D IR correlation spectra involves the production of short, transform-limited mid-IR pulses and the careful propagation and manipulation of these pulses through a five-beam interferometer to measure the third-order nonlinear rephasing and nonrephasing signals. These experiments typically use near-transform-limited, 90-fs pulses centered at 2050 cm^{-1} (4.9 μm), as illustrated in Figure 8. The generation and compression of mid-IR pulses at a 1-kHz repetition rate has been described in detail elsewhere.[90] However, it is important to note that experiments with optimally compressed pulses at the sample position require the design of an interferometer that effectively nulls the dispersion experienced by the IR fields to second order. The IR pulse is overlapped with

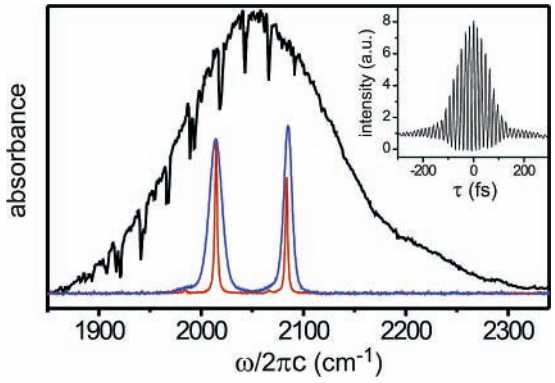

Figure 8. Typical pulse spectrum centered at 2050 cm^{-1} with a fwhm of 160 cm^{-1}. Underneath the spectral envelope is the linear FTIR spectrum of RDC in hexane (red) and in chloroform (blue) showing the two fundamental asymmetric and symmetric transition frequencies at 2015 and 2084 cm^{-1}. The full width half-maxima of the asymmetric and symmetric vibrational lines are 2.6 cm^{-1} in hexane and 14.6 and 9.3 cm^{-1} in chloroform, respectively. The inset shows an interferometric autocorrelation of a nearly transform-limited 90-fs mid-IR pulse.

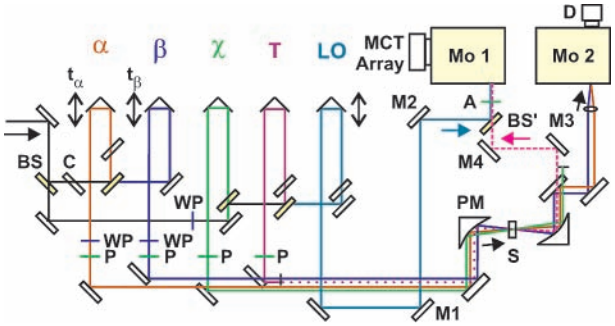

Figure 9. Experimental layout of the five-beam IR interferometer showing the three input pulses α, β, and χ and the tracer (T) and the LO pulse. M, gold-coated mirror; BS, 50−50, 4-mm-thick ZnSe beam splitter; C, 4-mm-thick ZnSe compensation plate; RR, 2 in. cube retroreflectors; PM, 10-cm focal length parabolic mirrors; WP, 2-mm-thick MgF_2 wave plates; P, wire-grid ZnSe polarizers; S, sample; BS′, 4-mm-thick ZnSe plate (AR coated on one side, uncoated on the other); A, analyzer; Mo, monochromator; and D, single-channel HgCdTe detector.

a mode-matched He−Ne beam using a Ge Brewster window (Infrared Optical) to simplify the alignment of the IR through the five-pulse interferometer. Following the overlap, the pulses are expanded and collimated in an all-reflective 1:2 telescope as described in an earlier publication.[52] The resultant near-transform-limited pulses entering the multibeam interferometer illustrated in Figure 9 are vertically polarized and are 12 mm in diameter.

The incoming beam is split into three input beams $\mathbf{E}_\alpha$, $\mathbf{E}_\beta$, and $\mathbf{E}_\chi$ of equal intensity using 50−50 4-mm-thick ZnSe beam splitters (Rocky Mountain Instrument Co.). The remaining fourth beam is split into a local oscillator and a tracer beam. The tracer, which is used for rough alignment and pump−probe experiments, follows the path of the signal and is blocked during the collection of the 2D data. The intensity and polarization of each of these five beams are controlled using a zeroth-order 2-mm-thick MgF_2 half-wave plate (Karl Lambrecht Corp.) followed by a 2-mm-thick ZnSe wire-grid polarizer (Molectron Detector, Inc.). The optical material in each arm of the interferometer is balanced by using 4-mm ZnSe compensation plates (Rocky Mountain Instrument Co.). The three input beams, each with

~50 nJ of energy, are incident on the sample in a box geometry and are focused to 150-μm spot sizes using a 100-mm focal length off-axis parabolic mirror (Janos Technology Inc.). To ensure optimal overlap at the sample, the three beams are put through a pinhole placed at the focus of the beams. Zero timing between the three input and tracer beams is set to within $\pm$5 fs by taking background-free intensity autocorrelations of each pulse pair in a 0.5-mm-long type I $AgGaS_2$ crystal (Eksma Co.) placed at the focal plane. The relative timing between the input pulses is controlled by 2-in. cube retroreflectors (PLX Inc.) mounted on a stepper-motor-driven linear stage (Newport) with 0.1-μm (0.667-fs) resolution and a repeatability of 1.5 μm (10 fs). For the rephasing experiments, $\mathbf{E}_\alpha$ is followed by $\mathbf{E}_\beta$ and then $\mathbf{E}_\chi$, and in the nonrephasing experiments, $\mathbf{E}_\beta$ enters the sample initially, followed by $\mathbf{E}_\alpha$ and $\mathbf{E}_\chi$. Before entering the interferometer, the IR beam is polarized in the vertical direction (*Z*) of the laboratory frame. Polarization-selective 2D IR spectra are collected at two polarization geometries *ZZZZ* (parallel) and *ZZYY* (crossed) by changing the input polarization of beams $\mathbf{E}_\alpha$ and $\mathbf{E}_\beta$. The waveplates in these two arms are adjusted to ensure that the same input energy reaches the sample in the two polarization geometries.

The third-order nonlinear rephasing and nonrephasing signals are generated in the phase-matched direction, $\mathbf{k}_s$, as shown in Figure 3. To characterize the nonlinear signal field completely, it is overlapped temporally and spatially with a local oscillator (LO). After passing through an analyzing polarizer (A), the two fields are dispersed in a monochromator, Mo 1 (Spex Industries Inc.), equipped with a liquid-nitrogen-cooled 64-element MCT array detector (IR Associates, Inc.; each pixel is 0.1 mm wide with a height of 1 mm). The initial spatial and temporal overlap is performed using the tracer (which follows the signal path) and the LO. The LO is spatially overlapped with the tracer on a 4-mm ZnSe window (BS′) using two irises separated by a distance of 1 m that monitor the intensity of IR light detected by a single-channel liquid-nitrogen-cooled MCT detector (Electro-Optical Systems Inc.). The timing between the LO and the tracer is set by monitoring their interference on a single-channel MCT detector placed before the monochromator. We noticed that the tracer beam does not always follow the same path as the emitted signal field, and adjustments need to be made in the signal and LO arms to ensure complete spatial overlap at the focal plane of the array detector. This is done by introducing a 1$-$2 ps delay (τ_3) between the LO and the signal fields with the help of a retroreflector mounted on a computer-controlled delay stage. The spectral interferogram of the signal and LO detected at the focal plane of the monochromator displays interference fringes whose frequency spacing reflects the value of the delay τ_3. The spatial overlap of the local oscillator and signal fields are adjusted using the mirror pairs M1, M2 and M3, M4, respectively, to increase the depth of the interference fringes in the spectral interferogram. Once optimal spatial overlap is achieved, the position of the LO is moved to set $\tau_3 = 0$ as previously determined from the interference between the tracer and LO fields in an earlier step. We are able to set the τ_3 delay to within $\pm$25 fs using this method. The spectral resolution in the ω_3 dimension is dictated by the entrance-slit width of the monochromator (150 μm), the linear dispersion at the focal plane, which is determined by the groove density of the grating, and the pixel width on the array detector (100 μm). Two different gratings with groove densities of 150 lines/mm and 90 lines/mm corresponding to spectral resolutions of ~1.3 and ~3 cm^{-1} are used for experiments on RDC dissolved in hexane and chloroform, respectively.

The MCT array detector is accompanied by a high-speed signal acquisition system and data acquisition software (Infrared Systems Development Corporation) that samples the data from the array detector at the 1-kHz pulse repetition rate. A LabView routine is used to collect arrays of spectrally dispersed heterodyne-detected rephasing and nonrephasing signals as a function of τ_1 by moving the computer-controlled translation stages for $\mathbf{E}_\alpha$ and $\mathbf{E}_\beta$. The data for RDC in hexane (chloroform) is collected by stepping the time delay τ_1 in steps of ~2 fs up to $\tau_1 = 8(4)$ ps. A mechanical chopper operating at 500 Hz chops beam $\mathbf{E}_\alpha$, and differential detection of the spectral data at the chopping frequency allows us to isolate the heterodyned signal of interest. Our experimental signal-to-noise ratio is determined by the noise on our LO. We adjust the intensity of the LO to be 10 times the signal intensity for the heterodyne detection scheme described above. For a particular value of τ_2, we collect the rephasing and nonrephasing signals followed by a dispersed pump$-$probe using the tracer as the probe and the beam $\mathbf{E}_\alpha$ as the pump beam. The room-temperature 1×10^{-3} and 5×10^{-3} M samples of RDC dissolved in hexane and chloroform are held in a stationary 200-μm-thick CaF_2 cell with 4-mm-thick windows corresponding to a peak optical density of 0.25. We collected 2D IR correlation spectra of RDC in chloroform for waiting periods of $\tau_2 = 0$, 1.4, 2.9, 6.2, and 9.5 ps.

In our previously published data,[52,53] we noticed distorted line shapes and an incorrect determination of resonant frequencies sampled during the evolution period, which hinders the interpretation of the resultant 2D spectra. These effects result from an improper calibration of the τ_1 axis due to the limitations of the stepper-motor-driven linear stages. To remedy this problem, the τ_1 timing was determined externally to within $\pm$1 fs by overlapping pulses $\mathbf{E}_\alpha$ and $\mathbf{E}_\beta$ after the sample and dispersing them in a $^1/_4$-m homebuilt monochromator (Mo2) with 100-μm-wide entrance and exit slits and a 300 lines/mm grating. Interference fringes collected at 1975 cm^{-1} as a function of the τ_1 delay are used to calibrate the τ_1 axis. We have tested our calibration method by performing a linear FID measurement of RDC dissolved in chloroform and have compared the resultant Fourier-transformed line shapes with an absorption spectrum from a commercial FTIR spectrometer. Using the calibration technique described above, the line shapes obtained after a Fourier transform of the FID data matched the FTIR spectrum within experimental noise.

VI. Data Analysis

The detection monochromator effectively performs a cosine transform of the overlapped signal and local oscillator fields, and we detect the interference term of interest by chopping one of the input beams as described in the previous section. In the limit where $|\mathbf{E}_{LO}|^2 \gg |\mathbf{E}_{sig}|^2$, the cosine transform of the interference term can be written as

$$\mathbf{O}(\mathbf{k}_s, \omega_t, \tau_3, \tau_2, \tau_1) = \int_0^\infty \mathbf{E}_{sig}(\mathbf{k}_s, t, \tau_2, \tau_1)\, \mathbf{E}_{LO}(\mathbf{k}_s, t - \tau_3) \cos(\omega_t t)\, dt \quad (17)$$

In the above expression, ω_t is the frequency of the dispersed signal and local oscillator fields. The delay τ_3 is approximately set to zero as explained in the previous section. Note that the desired interference term as written in eq 17 is not what the detector sees. Instead, the array detector measures the intensity of the light fields integrated over the width of the pixel ($2\Delta\omega$). Furthermore, the intensity of the detected light field is a

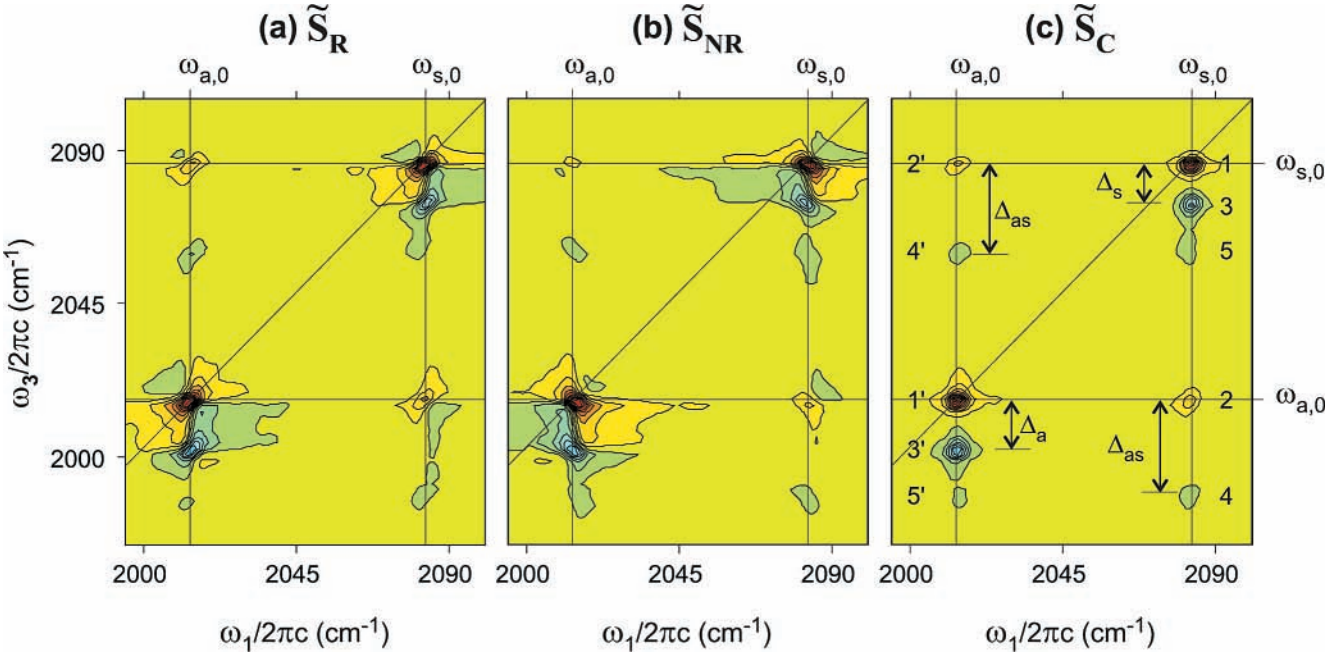

Figure 10. (a) Two-dimensional IR rephasing spectrum, (b) 2D IR nonrephasing spectrum, and (c) their sum, the 2D IR correlation spectrum, for RDC in hexane at $\tau_2 = 0$. These spectra were obtained in the all-parallel geometry. Fifteen equally spaced contour levels from the minimum to the maximum value are drawn for each 2D plot.

convolution of the desired signal with an instrument response function, $W(\omega_t)$, as shown below,

$$\mathbf{S}(\mathbf{k}_s, \omega_3, \tau_2, \tau_1) = \int_{\omega_3 - \Delta\omega}^{\omega_3 + \Delta\omega} \mathbf{O}(k_s, \omega_t, \tau_2, \tau_1) \otimes W(\omega_t)\, \mathrm{d}\omega_t + c.c. \quad (18)$$

The instrument response function depends on the characteristics of the monochromator such as the entrance-slit width, focal length, and diffraction grating. As a result, the data is sampled as an array of discrete frequencies ω_3 for a particular τ_1 delay. It is important to note that this array is equally spaced in wavelength but not in frequency. The issues of spectral resolution and unequal sampling in spectral interferometry have been the subject of a recent publication by Dorrer et al.[91]

The signal expressed by eq 18 is depicted as a function of ω_1 and ω_3 after a Fourier cosine transform of the data along the evolution time period:

$$\tilde{\mathbf{S}}(\mathbf{k}_s, \omega_3, \tau_2, \omega_1) = 2\int_0^{\infty} \mathbf{S}(\mathbf{k}_s, \omega_3, \tau_2, \tau_1^*) \cos(\omega_1 \tau_1^*)\, \mathrm{d}\tau_1^* \quad (19)$$

Before performing the Fourier cosine transform on the data, the original τ_1 axis is calibrated and interpolated to equally spaced time points represented by τ_1^* in the above equation. The interpolated data is multiplied by a triangular apodization function of the same length. This ensures that the data set decays smoothly to zero and that there are no spectral artifacts present after performing the Fourier transform. Finally, the data is zero padded to a length of 2^{15} elements, and then a Fourier transform is performed, resulting in a spectral resolution of 1 cm^{-1} in the ω_1 dimension. We notice that using the apodization function has a slight effect on the 2D line shapes. To nullify this effect, we multiply our calculated signals used to fit the experimental data with the same apodization function to extract correct linewidth parameters. Because the monochromator performs the Fourier cosine transform along τ_3, the 2D rephasing and nonrephasing spectra obtained after the transform along τ_1 (eq 19) appear in the ($\pm\omega_1$, $+\omega_3$) and ($\pm\omega_1$, $+\omega_3$) quadrants.

The resultant 2D rephasing $\tilde{\mathbf{S}}_R$ and nonrephasing spectra $\tilde{\mathbf{S}}_{NR}$ are added to produce a 2D correlation spectrum $\tilde{\mathbf{S}}_C$. It is important to note that we do not know the *absolute* phase of the signal represented by this 2D correlation spectrum. This is a result of our inability to determine the absolute zero timing between the input pulses ($\tau_1 = \tau_2 = 0$), the error in our ability to set $\tau_3 = 0$, and phase errors introduced by slight optical imbalances in the interferometer arms. To correct for the nonzero timings, we need to "phase" the 2D correlation spectrum in the ω_1 and ω_3 dimensions. It has been shown using the projection-slice theorem for 2D Fourier transforms that the projection of a 2D IR correlation spectrum at a particular τ_2 delay onto the $\omega_1 = 0$ axis is equal to the dispersed pump−probe signal measured for the same τ_2 value.[21] We make use of this fact to determine the correct phase of our nonlinear signal. This is done by multiplying the rephasing and nonrephasing spectra by a factor of $\exp[-i\omega_1\Delta\tau_1 - i\omega_3\Delta\tau_3 + i\phi]$ to obtain absorptive spectral features for slices $\omega_3 = \omega_{a,0}$ and $\omega_3 = \omega_{s,0}$ and to fit the projection of the 2D IR correlation spectrum to the particular dispersed pump−probe measurement. Note that this phasing procedure accounts for timing errors in τ_3 when making use of the projection slice theorem. The phasing in the ω_1 dimension to correct for timing errors in τ_1 assumes that the 1D line shapes along the fundamental frequencies are absorptive, which is not strictly true. We notice that values of ±4 fs are generally needed to phase the 2D spectra, accounting for the experimental timing errors ($\Delta\tau_1$ and $\Delta\tau_3$).

VII. Characteristics of 2D IR Correlation Spectra

Figure 10 shows the "phased" 2D rephasing $\tilde{\mathbf{S}}_R$, nonrephasing $\tilde{\mathbf{S}}_{NR}$, and correlation spectra $\tilde{\mathbf{S}}_C$ of RDC in hexane at $\tau_2 = 0$. The rephasing and nonrephasing spectra exhibit phase-twisted line shapes elongated along the diagonal ($\omega_1 = \omega_3$) and the off-diagonal ($\omega_1 + \omega_3 =$ constant) axes, respectively. Their sum is the absorptive 2D IR correlation spectrum, where the dispersive lobes are canceled from the addition of the 2D rephasing and nonrephasing spectra. The 2D correlation spectrum of RDC in hexane depicts 10 resonances with varying

signs, amplitudes, and tilts. We will refer to the different peaks in the 2D IR correlation spectrum as lying along the diagonal and off-diagonal axes according to their numbering scheme displayed in Figure 10c. In particular, peaks 1(1′) and 2(2′) are referred to as the diagonal and cross peaks, respectively.

Any nonlinear response for a purely harmonic system is zero. This implies that the very existence of a third-order material response requires vibrational interactions, which include (1) anharmonicity in the ground-state potential, (2) a nonlinear dependence of the transition dipole moment on the vibrational coordinates, or (3) nonlinear coupling in the system−bath interactions.[54,55,78,92] These effects are reflected in the positions, amplitudes, and line shapes in the 2D IR correlation spectrum. The positions of the peaks describe the transition frequencies of the vibrational eigenstates of the system. The peak amplitudes reflect the relative magnitudes and orientations of the transition dipole moments in the microscopic frame. The 2D line shapes are determined by the details of the system−bath interactions, which could result in the statistical variation of the eigenenergies in systems with coupled transition dipoles. These three observables functionally give a detailed characterization of the system eigenstates and the system−bath interactions, which will form the basis for modeling transient molecular structure and solvation dynamics. Here we will use 2D IR correlation spectra of RDC dissolved in hexane to characterize the energies and transition dipoles of the system eigenstates. The interaction of RDC with hexane is weak, allowing the solvation dynamics to be treated in the homogeneous limit. This is not the case for RDC dissolved in chloroform, and its 2D correlation spectra describe the effects of solvation dynamics on 2D line shapes.

A. Position and Sign of Resonances. The position of resonances in the 2D spectrum of RDC is dictated by the consecutive interactions of the multilevel vibrational system with a sequence of three electric fields. The ω_1 axis represents the frequency of the vibrational coherences excited after the first field−matter interaction; therefore, all the peaks in this dimension lie along the fundamental transitions: $\omega_1 = \omega_{a,0}$ and $\omega_1 = \omega_{s,0}$. The ω_3 axis indicates the state of the system after the third interaction, and we observe six possible resonance frequencies corresponding to the six transitions shown in the vibrational energy-level diagram of RDC in Figure 2. The diagonal peaks 1 and 1′ in Figure 10 represent four field interactions with the fundamental transitions, whereas cross peaks 2(2′) involve the transfer of coherence from one fundamental transition to the other. The remaining, oppositely signed peaks involve signals radiated from coherences involving the two-quantum states. For example, peak 3 (shifted below the diagonal peak) arises from a transition between the symmetric overtone (2s) and its fundamental (s), whereas peak 4 (shifted below cross-peak 2) arises from a transition involving the combination band (as) and the symmetric fundamental (s). The specific time-ordered interaction sequences contributing to the formation of each of these 10 peaks can be obtained by expanding the double-sided Feynman diagrams in Figure 5 in terms of the six eigenstates of RDC. This expansion leads to a total of 66 diagrams, when considering all of the possible transitions resonant with the mid-IR fields including the harmonically allowed one-quantum and the harmonically forbidden three-quantum transitions. (These diagrams are presented in Supporting Information.[73])

The positions of the peaks characterize the anharmonic nuclear potential of the coupled asymmetric and symmetric carbonyl stretches. The splittings between the labeled peaks correspond to anharmonic frequency shifts of the overtones ($\Delta_a = 14$ cm $^{-1}$, $\Delta_s = 11$ cm $^{-1}$) and the combination band ($\Delta_{as} = 26$ cm $^{-1}$). The signs of the peaks indicate whether the system evolves in a superposition of the fundamental and the ground state (positive) or in a superposition of the fundamental and doubly excited states (negative) during the detection period. The observed peak splittings in the 2D spectrum are related to the anharmonic expansion terms in the nuclear potential describing the coupled carbonyl stretches using normal or local vibrational coordinates.[7,54] In the limit of a harmonic nuclear potential, $\Delta_a = \Delta_s = \Delta_{as} = 0$, and oppositely signed resonance peaks 3 and 5 would lie on top of peak 1 and peak 4 would lie on top of peak 2. These peaks would destructively interfere, leading to a decrease in or the disappearance of the peaks in the 2D spectrum. This explains the appearance of cross peaks for coupled vibrations. For two uncoupled vibrations, the off-diagonal anharmonicity $\Delta_{as} = 0$, and the cross peak vanishes because of destructive interference between pathways that lead to peaks 2 and 4. The presence of 10 distinct peaks in the 2D IR correlation spectrum of hexane indicates that there is a nonlinear dependence (cubic and higher) of the nuclear potential on the vibrational coordinates, which satisfies the first selection rule for 2D IR spectroscopy.

B. Peak Amplitudes. Although the positions of the peaks in a 2D IR correlation spectrum are dictated by the transition frequencies between system eigenstates probed by the sequence of external fs fields, their amplitudes are determined by the relative strength and direction of the four interacting transition dipoles. An analysis of the relative peak amplitudes reveals (1) information about the projection angle between transition dipoles of the eigenstates and (2) the presence of electrical anharmonicity in the system or the nonlinear dependence of the transition dipole moments on the vibrational coordinates. Such an analysis requires separating the nonlinear vibrational and orientational response functions because they contain complementary information about the amplitudes and relative angles of the transition dipoles, respectively.

To separate out these two contributions, we measure the 2D IR correlation spectra in two different polarization geometries, which sample response functions differing only in the orientational factors, Y_{IJKL}. For a particular resonance, the ratio of its amplitude from two different geometries yields information about the angle(s) between transition dipoles involved in its formation. In the case of cross peaks, this gives direct information on the projection angle between two coupled transition dipole moments.[64]

The effects of electrical anharmonicity are revealed by comparing the ratio of the amplitudes of oppositely signed peak pairs in 2D IR correlation spectra collected in two different polarization geometries. For a linear dependence of the dipole moment on the vibrational coordinate, the transition dipole moment amplitudes connecting the zero- (0-) and one- (1-) quantum states $\mu^{1,0}$ to those connecting the one- and two- (2-) quantum states $\mu^{2,1}$ follow harmonic scaling, and $\mu^{2,1} = \sqrt{2}\,\mu^{1,0}$. In this limit, the amplitudes of the oppositely signed peak pairs, 1 and 3 or 2 and 4, would be equal. A nonlinear dependence of the transition dipole vectors on the vibrational coordinates results in the variation of the amplitude in these peak pairs.

The second row in Figure 11 shows polarization-selective 2D IR correlation spectra of RDC in hexane collected in the $Z - Z - Z - Z$ and $Z - Z - Y - Y$ polarization geometries ($\alpha-\beta-\chi-$sig). We refer to these as the parallel $\tilde{\mathbf{S}}_{\parallel}$ and crossed $\tilde{\mathbf{S}}_{\perp}$ 2D IR correlation spectra. Because these spectra are collected for $\tau_2 = 0$, the time-ordering (1−2−3) of pulses $\alpha - \beta - \chi$ and $\alpha - \chi - \beta$ are indistinguishable for the rephasing experiment. This implies that the rephasing experiment in the

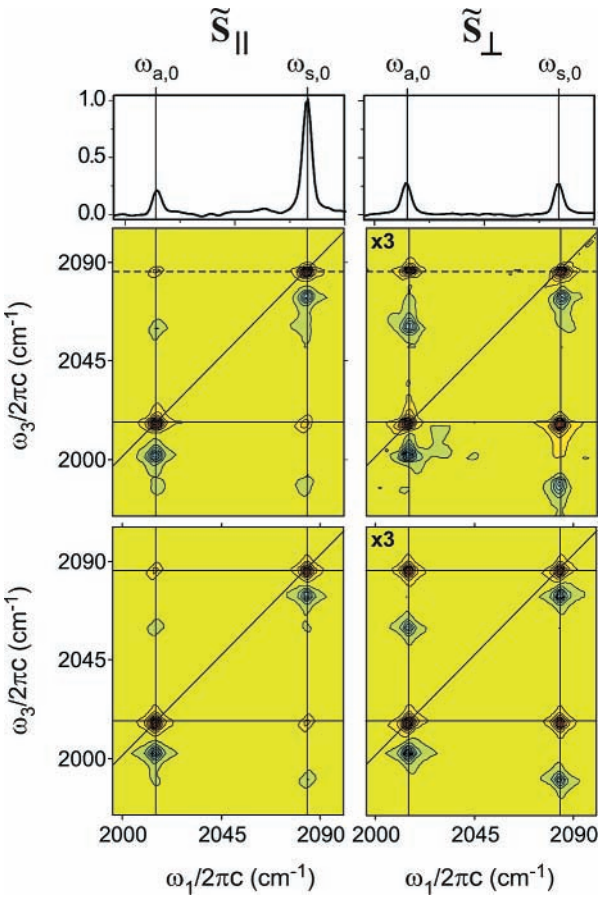

Figure 11. Experimental and calculated 2D correlation spectra obtained in the *ZZZZ* and *ZYYZ* polarization geometries for RDC in hexane at $\tau_2 = 0$. The middle row shows the experimentally collected 2D correlation spectra. Slices from these spectra taken at $\omega_3 = \omega_{s,0}$ are shown in the top panel. The bottom row depicts the calculated 2D spectra using the eigenstate parameters obtained from the best-fit results. Twenty-one equally spaced contour levels from the minimum to the maximum value are drawn for each 2D plot.

crossed polarization geometry samples both the Y_{ZZYY} and Y_{ZYZY} tensor elements of the S_I response function. Similarly, the pulse sequences $\beta - \alpha - \chi$ and $\beta - \chi - \alpha$ cannot be separated in the nonrephasing experiment for $\tau_2 = 0$, and the nonrephasing experiment samples the Y_{ZZYY} and Y_{ZYZY} tensor components of the S_{II} and S_{III} responses, respectively.

The peak positions in each of the polarization-selective spectra are identical; however, the relative amplitudes and tilts of the various peaks are different. The ratios of the amplitudes of the cross peaks to the diagonal peaks are approximately $\sim 1/4$ and ~ 1 in the 2D spectra obtained in the parallel and crossed polarization geometry, respectively. Additionally, the diagonal amplitude of the crossed-polarized 2D spectra is $\sim 1/4$ that of the spectrum obtained in the all-parallel geometry.

The dependence of the amplitude ratios for a particular peak in the two experiments ($A_\perp/A_{||}$) can be related to the projection angle between the two fundamental transitions, Θ, using the orientational response functions contributing to a particular peak.[64,65] Figure 12 shows a plot of $A_\perp/A_{||}$ as a function of Θ for the diagonal and cross-peak amplitudes in the 2D IR correlation spectra between the transition dipoles of two vibrational modes. As the angle between the dipole varies from parallel to orthogonal, the cross-peak ratio varies from $1/3$ to $7/6$, and the diagonal peak ratio varies from $1/3$ to $6/23$. The calculation in Figure 12 is for the case $\tau_2 > 0$, but it also holds at $\tau_2 = 0$ provided that the transition dipole vectors $\hat{\boldsymbol{\mu}}^{1,0}$ and

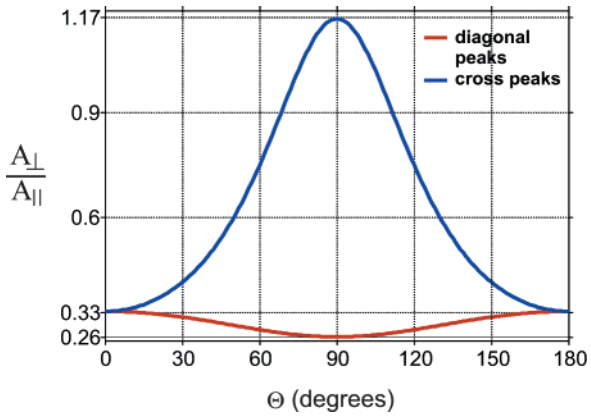

Figure 12. Ratio of the diagonal and cross-peak amplitudes ($A_\perp/A_{||}$) in the 2D IR correlation spectra obtained in the parallel and crossed-polarization geometries as a function of the angle Θ between the transition dipoles of two coupled vibrational modes. The plot is shown for the case when $\tau_2 > 0$, but it also holds at $\tau_2 = 0$ provided that the transition dipole vectors $\hat{\boldsymbol{\mu}}^{1,0}$ and $\hat{\boldsymbol{\mu}}^{2,1}$ are parallel to each other.

$\hat{\boldsymbol{\mu}}^{2,1}$ are parallel to each other. The latter assumption is nearly true for our present case because of the intrinsic symmetry of the molecule. A comparison of the amplitudes of the cross and diagonal peaks from the slices along $\omega_3 = \omega_{s,0}$ plotted on the first row of Figure 11 reveals ratios of ~ 1 and $\sim 1/4$, respectively, indicating that the transition dipole vectors of the coupled asymmetric and symmetric stretches are orthogonal.

In addition to revealing the angle between the coupled carbonyl stretches, a comparison of the polarization-selective spectra indicates the presence of electrical anharmonicity. In the experimental 2D spectra of Figure 12, we notice that the amplitude of peak 1 is greater than that of the negatively signed peak 3, and this ratio of amplitudes is unchanged with different polarization geometries. Similarly, the amplitude of peak 2 is greater than that of peak 4. These observations imply that $\mu^{2s,s} \neq \sqrt{2}\,\mu^{s,0}$ and $\mu^{as,a} \neq \mu^{s,0}$. The effects of electrical anharmonicity on the peak amplitudes of 2D IR spectra have been treated in detail in ref 54. The presence of electrical anharmonicity for a mechanically harmonic system ($\Delta_a = \Delta_s = \Delta_{as} = 0$) ensures that the interference between pathways involving only the fundamental states and those involving the two-quantum states will be incomplete, resulting in the nonzero amplitude of the 2D IR correlation spectrum. Generally, both electrical and nuclear anharmonicity result in a deviation from harmonic scaling for the amplitudes of $\boldsymbol{\mu}^{1,0}$ and $\boldsymbol{\mu}^{2,1}$ and also make these two transition dipoles noncollinear with respect to each other.

It is important to note that the amplitude of peaks in the 2D IR spectrum are affected by relaxation processes during all three time variables. Coherent and incoherent population relaxation or exchange processes lead to a change in peak amplitudes both through changes in amplitude in the density matrix elements for the system arising from these relaxation processes[34] and also through changes in the orientational projections of the fields onto the dynamically evolving system. These effects are not discussed explicitly here but are the subject of ongoing work.

C. 2D IR Line Shapes. The line shape of a given resonance in a 2D IR spectrum reflects the effects of the bath on the four interacting transition dipoles. Here, we will restrict ourselves to exploring only the effects of vibrational dephasing on the 2D IR line shape based on a linear interaction between the system and bath coordinates. Within this model, the 2D line shape allows us to describe quantitatively the time scales of the transition frequency fluctuations by characterizing the system−bath correlation functions ζ.[35,48] This can be illustrated

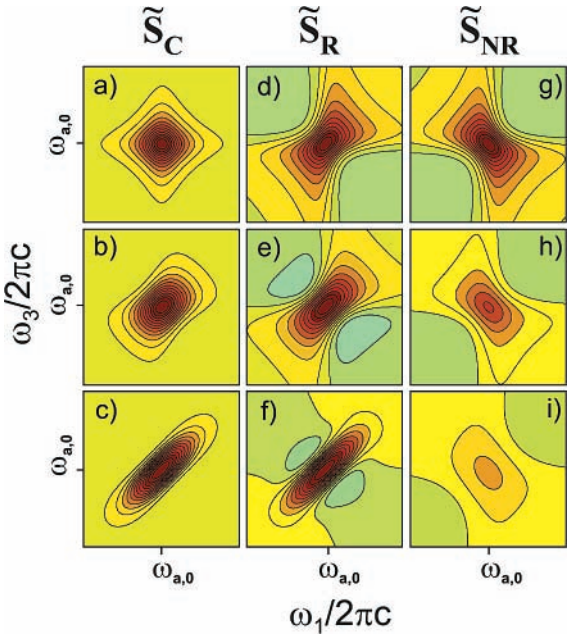

Figure 13. Characteristic 2D line shapes for a two-level system undergoing stochastic modulation of the transition frequency $\omega_{a,0}$ whose correlation function is defined as $\langle \delta\omega_{a,0}(t)\ \delta\omega_{a,0}(0)\rangle = \sigma^2 e^{-t/\tau_c}$ with fluctuation amplitude σ and correlation time τ_c. The spectral line shapes describe the limits of fast fluctuations or the low-amplitude regime (homogeneous, $\sigma\tau_c = 0.1$) (a, d, and g), the intermediate regime ($\sigma\tau_c = 1$) (b, e, and h), and the slow fluctuations (inhomogeneous, $\sigma\tau_c = 10$) regime (c, f, and i). The labels $\tilde{\mathbf{S}}_C$, $\tilde{\mathbf{S}}_R$, and $\tilde{\mathbf{S}}_{NR}$ correspond to 2D correlation, rephasing, and nonrephasing spectra, respectively. Note that as the system−bath interaction dynamics move from the fast to the slow limit the 2D line shape goes from being symmetric (a) to being diagonally elongated (b, c). Also, the relative amplitudes of the rephasing spectra (d−f) increase with respect to those of the nonrephasing spectra (g−i). The contours are plotted at 8% intervals.

through calculations of the 2D line shape for a two-level system using a stochastic model for the frequency fluctuations. In this model, the transition frequency fluctuates with an amplitude σ and a characteristic correlation time τ_c and $\zeta(\tau) = \sigma^2 \exp(-\tau/\tau_c)$. This model can be continuously varied between the homogeneous ($\sigma\tau_c \ll 1$) and inhomogeneous ($\sigma\tau_c \gg 1$) limits of the system−bath dynamics.[93]

Figure 13 shows simulations of the 2D line shape for a two-level system within this stochastic model for different values of $\sigma\tau_c$ varying from homogeneous to inhomogeneous. For $\sigma\tau_c = 0.1$ (Figure 13a), the 2D correlation spectrum shows a homogeneously broadened, symmetric diamond line shape. The homogeneous limit implies that the time scale of the energy gap fluctuations are fast compared to the experimental time scales τ_1, τ_2, and τ_3. This results in exponential dynamics during τ_1 and τ_3, which are reflected by the diamond-shaped line.[42,46] When the system−bath dynamics are homogeneous, the rephasing (Figure 13d) and nonrephasing (Figure 13g) 2D spectra have the same amplitude and show the characteristic phase-twisted line shapes aligned along the diagonal and antidiagonal axes, respectively.[32,69] The degree of elongation of the line shape along the diagonal axis increases with increasing $\sigma\tau_c$ (Figure 13a−c).

Figure 13c shows the 2D correlation spectrum in the inhomogeneous limit ($\sigma\tau_c = 10$), where the experimental time scales are much shorter than the time scale of the transition fluctuations. For this limit, the ensemble can be described as a static distribution of homogeneous line shapes summed along the diagonal. The diagonal slice is representative of the width of the distribution (σ), whereas a slice along the antidiagonal is a measure of the homogeneous line width for the ensemble (σ^2/τ_c).[42,43] The rephasing and nonrephasing spectra in this limit are shown in Figure 13f and i, respectively. Because the individual homogeneous line shapes in the rephasing and nonrephasing 2D spectra lie along the diagonal and off-diagonal axes, respectively, the summation of contributions from the ensemble along the diagonal leads to constructive interference in the former case and destructive interference in the latter. This result explains the much higher intensity and diagonal elongation of the rephasing spectrum relative to the nonrephasing spectrum.[35,69] The inhomogeneity of the system can therefore be indirectly related to the relative amplitude of the rephasing (A_R) and nonrephasing spectra (A_{NR}). As defined in section IV, this ratio can be expressed as an angle Ψ given by $\tan(\Psi) = (A_R - A_{NR})/(A_R + A_{NR})$. These observations can also be explained from the dynamics of the ensemble in the time domain. In a rephasing experiment, the dephasing experienced by the static ensemble during τ_1 is rephased during τ_3 because of the conjugate nature of the phase acquired by the coherences in the two periods. This results in the formation of a strong echo when $\tau_1 = \tau_3$, the Fourier transform of which directly corresponds to the diagonally elongated 2D line shape in the rephasing spectrum. In the nonrephasing experiment, the decrease in the signal level during τ_1 due to inhomogeneous dephasing continues uninterrupted during τ_3, reflecting the low amplitude yet roughly symmetric line shape in Figure 13i. It should be noted that even though the rephasing and nonrephasing spectra in the inhomogeneous limit are of different amplitudes the dispersive components of their phase-twisted line shapes are still properly canceled in the 2D correlation spectrum (Figure 13c).

Following the above model calculations, the diamond-shaped peaks observed in 2D correlation spectra of RDC in hexane are indicative of a homogeneously broadened system where the rephasing and nonrephasing experiments sample the same dynamics. However, all of the peaks in the 2D IR correlation spectrum of Figure 10c do not have purely absorptive features, with some of the peaks retaining a partially phase-twisted character. We have shown elsewhere that in a multilevel vibrational system there is an inherent asymmetry in the rephasing and nonrephasing Liouville pathways contributing to the formation of the 10 resonances.[32,73] For example, in the case of peak 2(2′), there are twice as many rephasing pathways as nonrephasing pathways. Also, only nonrephasing pathways contribute to the formation of peak 5(5′). Using this information, we would predict that the 2D IR correlation spectrum would show peaks 2(2′) and 5(5′) tilted along the diagonal and off-diagonal axes, respectively, as indeed is the case. We see that the line shapes of peaks 2(2′) and 4(4′) are tilted by approximately $\pi/10$ from the ω_1 axis. However, peaks 1(1′) and 3(3′) are symmetric about the ω_1 axis and purely absorptive in nature, suggesting that they have equal amplitudes in the rephasing and nonrephasing 2D spectra. A comparison of the polarization-selective 2D IR spectra of RDC in hexane reveals how microscopic factors such as the tensor components measured in the rephasing and nonrephasing experiment affect the tilts of the various features in a 2D IR correlation spectrum for a homogeneously broadened system. In particular, we see that cross peaks in $\tilde{\mathbf{S}}_\perp$ are almost symmetric about the ω_1 axis and those in $\tilde{\mathbf{S}}_\parallel$ are phase-twisted and tilted toward the diagonal axis.

VIII. Modeling Transient Structure

The analysis of the positions, amplitudes, and line shapes of the various peaks in the 2D IR correlation spectra of RDC characterizes the system eigenstates and the specific system−

bath interactions of our six-level vibrational system. These observables allow us to model structure, understand the variation of molecular conformations, and follow the relaxation and conformational dynamics of molecules in the condensed phase on the time scale of our experiment. In the case of RDC dissolved in hexane where the interaction with the solvent is particularly weak and the individual line widths of the transitions are much narrower than the anharmonic frequency shifts, polarization-selective 2D IR spectra provide an intuitive mapping of the system eigenstates and reveal the orthogonal projection angle between the two transition dipole vectors of the symmetric and asymmetric states. These eigenstates are delocalized over the molecule; therefore, their characterization does not provide an immediate and obvious connection to local transient structure. Using a local-mode description, we can relate these eigenstate parameters to the coupling strength and angle between the C≡O bonds. The analysis builds on ref 52, where we extracted local-mode parameters of the same molecule from its absolute value 2D rephasing spectrum.

The 2D correlation spectra of RDC are modeled in terms of local carbonyl bond stretches with reduced vibrational coordinates $\mathbf{Q}_m$ and $\mathbf{Q}_n$. Their transition dipole vectors, $\boldsymbol{\mu}_m^{(1)}$ and $\boldsymbol{\mu}_n^{(1)}$, lie along the C≡O bond and are aligned at an angle θ with respect to each other. The bond stretch coordinates are represented as cubic anharmonic oscillators coupled through a bilinear interaction. The local vibrational system Hamiltonian $\tilde{H}_S^V$ is given below:

$$\tilde{H}_S^V(\mathbf{Q}_m,\mathbf{Q}_n) = \frac{1}{2}\hbar\omega_m^0\mathbf{Q}_n^{\,2} + \frac{1}{2}\hbar\omega_n^0\mathbf{Q}_n^{\,2} + V_{mn}\mathbf{Q}_m\mathbf{Q}_n + \frac{1}{6}(g_{mmm}\mathbf{Q}_m^{\,3} + g_{nnn}\mathbf{Q}_n^{\,3}) + \frac{\mathbf{P}_n^{\,2}}{2m} + \frac{\mathbf{P}_m^{\,2}}{2m} \quad (20)$$

In the above expression, the bilinear coupling constant is given by V_{ij} and the cubic anharmonic coefficients are represented by g_{iii}. Equation 20 assumes symmetry with respect to the order of indices m and n in the definition of the bilinear coupling constant.

The transition dipole vectors among the eigenstates are obtained by writing the dipole operator in terms of the local coordinates and performing the appropriate transformation to the eigenbasis. To account for the electrical anharmonicity observed in the experimental 2D correlation spectra, the dipole operator in the local basis $\tilde{\mathbf{M}}$, is expanded to the third order in each of the local vibrational coordinates as shown below,

$$\tilde{\mathbf{M}}(\mathbf{Q}_m, \mathbf{Q}_n) = \boldsymbol{\mu}_m^{(1)}\mathbf{Q}_m + \frac{1}{6}\boldsymbol{\mu}_{mmm}^{(3)}\mathbf{Q}_m^3 + \boldsymbol{\mu}_n^{(1)}\mathbf{Q}_n + \frac{1}{6}\boldsymbol{\mu}_{nnn}^{(3)}\mathbf{Q}_n^3 \quad (21)$$

In eq 21, $\boldsymbol{\mu}_m^{(1)}$ and $\boldsymbol{\mu}_m^{(3)}$ are the first- and third-order expansion coefficients of the dipole vector $\boldsymbol{\mu}_m$ evaluated at the equilibrium configuration. The second-order expansion is ignored because those dipole matrix elements do not contribute to the resonant transitions observed in this experiment. The transition dipole moments between the eigenstates of the system Hamiltonian H_S are obtained by performing the appropriate unitary transformation.

The parameters in the Hamiltonian $\tilde{H}_S^V$ describing the two local vibrations are found by fitting the experimental 2D correlation spectra $\tilde{\mathbf{S}}_{\|}$ and $\tilde{\mathbf{S}}_{\perp}$. We obtain analytical expressions for the observed signals following the procedure outlined in section III and assuming infinitely short input pulses. The fitting routine involves writing out the system Hamiltonian and dipole operator in the local basis using eqs 20 and 21 and accounting for vibrational states with 10 quanta of energy. The matrices are then transformed to obtain the eigenenergies, eigenvectors, and transition dipole vectors of the six lowest-lying vibrational states. Using the obtained eigenstate parameters, appropriate line-shape functions characteristic of a homogeneously broadened system, the correct orientational factors, and the 2D correlation spectra for the parallel and crossed polarization geometries are calculated. We assume that the parameters in the local Hamiltonian are invariant to indices m and n because of the intrinsic symmetry of the molecule in which the two carbonyl stretches are chemically equivalent. All of the dephasing constants are set equal to the value ($\Gamma_{pq} = \Gamma$), as indicated by the identical line widths of all the resonances in the 2D correlation spectra in both of the frequency dimensions. A total of six parameters are floated, including $\omega_m^0 = \omega_n^0$, V_{mn}, $g_{mmm} = g_{nnn}$, θ, $\mu_{mmm}^{(3)}/\mu_m^{(1)} = \mu_{nnn}^{(3)}/\mu_n^{(1)}$, and Γ. These parameters are refined to obtain the best fit to the experimental 2D spectra. In the above analysis, there are no assumptions made regarding the relative orientations of all six transition dipoles.

The nonlinear least-squares fitting of the experimental data resulted in the following values for the best-fit parameters: $\omega_m^0 = \omega_n^0 = 2074 \pm 1$ cm^{-1}, $V_{mn} = 35 \pm 0.5$ cm^{-1}, $g_{mmm} = g_{nnn} = 172 \pm 1$ cm^{-1}, $\theta = 91 \pm 1°$, $\mu_{mmm}^{(3)}/\mu_m^{(1)} = \mu_{nnn}^{(3)}/\mu_n^{(1)} = -0.4$, and $\Gamma = 2 \pm 1$ cm^{-1}. The 2D correlation spectra shown in the last row of Figure 11 are simulated using the results of the best fit and are successfully able to reproduce the positions, relative amplitudes, and line shapes of all of the resonances in the experimental spectra. All of the parameters of the local Hamiltonian and the eigenstates are tabulated in Table 19S of the Supporting Information. The bilinear coupling constant, frequencies, and cubic anharmonicities of the local stretches determine the accurate positions of the peaks in the 2D IR spectrum. The angle between the local stretches and the magnitude of the third-order coefficients of the dipole operator determine the relative amplitude of the 10 resonances in the 2D IR spectrum, and the value of Γ reflects the width of the 2D line shape in both dimensions.

The analysis reveals the accurate positions of the fundamental frequencies at $\omega_{a,0} = 2015$ cm^{-1} and $\omega_{s,0} = 2084$ cm^{-1}, and the corresponding anharmonic splittings of the higher-lying states Δ_a, Δ_s, and Δ_{as} are 14, 11, and 26 cm^{-1}, respectively. The value of Γ reflects the line width of the fundamental transitions obtained from linear FTIR measurements. The value of the angle, θ, between the transition dipoles of the two local modes was found to be $91 \pm 1°$ which affects the amplitudes of the transition dipoles between the fundamental eigenstates found to be $\mu^{s,0} = 0.9\mu^{a,0}$.[94] This result is consistent with previously measured 2D IR rephasing spectra and with data obtained from X-ray crystallography.[52,95] It should be noted here that because of the intrinsic symmetry of the molecule any value of θ would result in the two fundamental transition dipoles being mutually orthogonal.

The electrical anharmonicity of the local-mode transition dipoles results in the nonharmonic scaling of the amplitudes of the transition dipoles among the six eigenstates. For example, we note that $\mu^{2a,a} = \mu^{2s,s} = 1.2\mu^{a,0}$ and $\mu^{as,a} = \mu^{as,s} = 0.7\mu^{a,0}$ as reflected in the unequal amplitudes of the peak pair 1(1′) and 3(3′) and the pair 2(2′) and 4(4′) in the experimental 2D spectra. The fact that the observed amplitudes of the transition dipoles are less than their harmonic values is indicative of the negative value of $\mu_{mmm}^{(3)}$ and $\mu_{nnn}^{(3)}$. The amplitudes of the transition dipole moments between the eigenstates are also affected by the diagonal and off-diagonal cubic anharmonic terms, although to a lesser extent than the electrical anharmonicity. For instance,

if we set $\mu^{(3)} = 0$ leaving the other parameters the same, then the transition dipoles deviate from harmonic scaling by a maximum of 4%.

The above analysis also reveals the angles between the transition dipoles of the eigenstates connecting the zero- to one-quantum states ($\boldsymbol{\mu}^{1,0}$) and those connecting the one- to two-quantum states ($\boldsymbol{\mu}^{2,1}$), and the analysis and results are given in the Supporting Information. For a harmonic system, we would expect the two angles to be parallel to each other. Although we have an anharmonic system, we notice that the angles deviate very slightly from harmonic behavior. The slight discrepancy arises from the presence of the electrical anharmonicity. Because of the intrinsic symmetry of the molecule and the degeneracy of the two local stretches, the effects of mechanical anharmonicity on the amplitudes and relative orientations of $\boldsymbol{\mu}^{1,0}$ and $\boldsymbol{\mu}^{2,1}$ are negligible. Ongoing studies of 2D IR spectra of RDC in hexane collected as a function of the waiting period provide evidence of coherence transfer and incoherent population transfer among the two-coupled symmetric and asymmetric eigenstates. These relaxation processes will affect the determination of angles between the two coupled vibrations and affect the parameters in the local Hamiltonian as well as the electrical anharmonicity of the local transition dipole operator.

A more detailed picture of molecular structure from the above analysis requires an understanding of the vibrational coupling mechanism. The extent to which this is understood directly determines the type of structural information that can be accessed through 2D IR spectroscopy. Generally speaking, "through-bond" and "through-space" interactions between two vibrational coordinates will affect the magnitude of their coupling. For through-bond covalent interactions, couplings can be related to connectivity. The electrostatic through-space interactions have well-defined distance scaling relationships and can potentially relate couplings to intra- and intermolecular distances. For the particular case of the strongly coupled vibrations in RDC, the coupling is thought to arise from covalent interactions of the carbonyl groups with the Rh metal center primarily through $d_\pi - \pi^*$ back-bonding effects.[96] In the case of weakly coupled amide I vibrations in small peptides, the coupling has been modeled in terms of through-space Coulombic interactions.[37,97,98] Recent ab initio studies on the coupling between the amide I modes of a glycine dipeptide analogue reveal that one needs to account for through-bond effects characterizing the anharmonicity of the nuclear potential along with couplings between a distribution of transition charges to obtain quantitative agreement with experimental results.[7,99,100]

IX. Correlated Dynamics from 2D Relaxation Experiments

In the preceding sections, we have focused on the sensitivity of the 2D IR correlation spectroscopy to the details of the system Hamiltonian, H_S. This molecular information has been primarily based on fitting the positions and amplitudes of resonances in polarization-selective 2D IR spectra. For RDC, the interactions with hexane are very weak, leading to the narrow, homogeneously broadened 2D line shapes. Therefore, the effects of the solvent on the solute's transition energies can be largely ignored, providing a convenient model system to describe with a single unique structure. In general, the system−bath interactions are stronger, and the effects of fluctuations of transition energies within an ensemble have to be taken into account. In this case, the 2D line shapes are the observable of interest for determining the time scale and magnitude of the solvation effects, as illustrated in Figure 13. For the dynamics of a system of coupled vibrations, we must additionally be concerned with the correlation between the fluctuations of different energy levels,[101−104] which is revealed in the 2D line-shape analysis of cross peaks.[35,69,105]

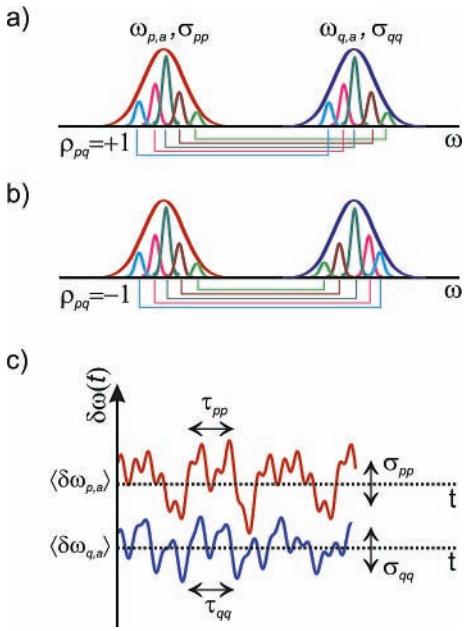

Figure 14. Schematic representation of the correlation of the bath-induced frequency shifts for system eigenstates p and q with eigenfrequencies $\omega_{p,a}$ and $\omega_{q,a}$. (a) Correlated ($\rho_{pq} = +1$) and (b) anticorrelated ($\rho_{pq} = -1$) joint distributions with inhomogeneous standard deviations of σ_{pp} and σ_{qq}. For $\rho_{pq} = +1$, the members within the joint inhomogeneous distribution are shifted equally from the central frequency such that $\omega_{p,a} - \omega_{q,a} = \omega^0_{p,a} - \omega^0_{q,a}$ when $\sigma_{pp} = \sigma_{qq}$. The shift is equal but occurs in the opposite directions for $\rho_{pq} = -1$ such that $\omega_{p,a} + \omega_{q,a} = \omega^0_{p,a} + \omega^0_{q,a}$. (c) Time-dependent frequency fluctuations with arbitrary correlation. The variables $\tau_{pp(qq)}$ and $\sigma_{pp(qq)}$ are the fluctuation correlation time and fluctuation amplitudes parameters of the stochastic Kubo line-shape model, respectively. For more details, see the text.

A. Correlated Transition-Energy Shifts. For two coupled vibrations p and q, the nature of the microscopic system−bath interactions and the way in which they affect the coupling may lead to a statistical interdependence between the individual transition shifts $\delta\omega_{p,a}$ and $\delta\omega_{q,a}$. For two static distributions characterized by standard deviations σ_{pp} and σ_{qq}, this effect can be characterized by a correlation coefficient ρ_{pq},

$$\rho_{pq} = \frac{\langle \delta\omega_{p,a}\delta\omega_{q,a}\rangle_B}{\sigma_{pp}\sigma_{qq}} \tag{22}$$

which is the normalized covariance of $\delta\omega_{p,a}$ and $\delta\omega_{q,a}$ over the ensemble [29,35,69,101,105−107]. ρ_{pq} can take on values between −1 and +1, where the magnitude of ρ_{pq} reflects the degree of correlation of the individual frequencies. As illustrated in Figure 14, when $\sigma_{pp} = \sigma_{qq}$, complete correlation ($\rho_{pq} = +1$) means that the shift from the central frequency for each member of the ensemble is the same ($\omega_{p,a} - \omega_{q,a} = \omega^0_{p,a} - \omega^0_{q,a}$). Similarly, $\rho_{pq} = -1$ is completely anticorrelated, indicating that the shift is equal but opposite ($\omega_{p,a} + \omega_{q,a} = \omega^0_{p,a} + \omega^0_{q,a}$).[107] In the case of complete correlation or anticorrelation, there exists a linear regression relationship between the frequency-shift variables such that $\delta\omega_{p,a} = \pm\delta\omega_{q,a}\sigma_{pp}/\sigma_{qq}$.

From the local-mode perspective, the relative energy shifts experienced by two vibrational transitions can be interpreted as arising from fluctuations in the local vibrational potential or

from fluctuations in the couplings between vibrations. In each case, the origin of the fluctuations directly influences the relative shifts in energy of the system eigenstates. If the interaction with the solvent leads to variation in the local vibrational potential (diagonal disorder) while the coupling remains constant, then the two transition energies will shift together, leading to correlated fluctuations ($\rho_{pq} > 0$). For variation in the coupling between vibrations, or off-diagonal disorder, interactions shift the transition frequencies of the coupled modes in an anticorrelated fashion ($\rho_{pq} < 0$).[38,103,108−110] The experimental distinction between correlated and anticorrelated broadening forms the basis for revealing whether the fluctuations arise from the solvent acting on the local potential or are of a conformational nature.[36,41,111]

Cross peaks in a 2D IR correlation spectrum arise from propagation under two different distributions during τ_1 and τ_3, and their line shapes are sensitive to the cross correlation of their transition frequency distributions. In the case of totally correlated broadening ($\rho_{pq} = +1$), the transition energy shift $\delta\omega_{p,a}$ corresponds to an equal shift in $\delta\omega_{q,a}$. In the process that forms a cross peak between $\omega_{p,a}$ and $\omega_{q,a}$, the phase acquired during the evolution period ($\omega_{p,a}\tau_1$) is transferred to the second transition so that the memory of the frequency in the evolution period is retained in the detection period. In a rephasing experiment, this process results in the focusing of the original polarization, and an echo forms on the second transition $\omega_{q,a}$. This echo formation leads to a cross peak that is elongated parallel to the diagonal peaks (Figure 15a). For totally anticorrelated broadening ($\rho_{pq} = -1$), the shift in energy of $\omega_{p,a}$ is opposite to the shift in $\omega_{q,a}$. In inducing a cross peak, the phase acquired by members of the distribution during τ_1 is transferred to the second distribution in an inverted manner. Macroscopic focusing of the initial coherence is not possible in the rephasing experiment because dephasing by the ensemble in the detection period continues. Thus, cross peaks will be suppressed in the rephasing spectrum (Figure 15d). However, the refocusing of the ensemble is seen in the conjugate, nonrephasing experiment because of the inverse frequency-shift relationship between $\omega_{p,a}$ and $\omega_{q,a}$. This leads to pronounced cross peaks in the nonrephasing spectrum (Figure 15d) that are elongated along the antidiagonal axis.[35,69] The 2D IR correlation spectrum combines the selectivity of rephasing and nonrephasing spectra to correlated and anticorrelated broadening (Figure 15c and f).[35] The ellipticity and direction of elongation of the cross peaks relative to the diagonal peaks gives a measure of the degree of correlation. This elongation can be quantified by the angle Ψ; $\tan(\Psi) = (A_R - A_{NR})/(A_R + A_{NR})$, where ($A_R$) and ($A_{NR}$) are the amplitudes of the various peaks in the rephasing and nonrephasing spectra, respectively.

The correlation effects can also be extended to time-dependent transition frequencies by building on the stochastic model[75,112] that was used to describe the line shapes in Figure 13. As pictured in Figure 14c, we can describe the fluctuations of two transition frequencies $\delta\omega_{p,0}$ and $\delta\omega_{q,0}$ with amplitudes σ_{pp} and σ_{qq}, each with a characteristic correlation time. We model the time-dependent system−bath dynamics by an exponentially decaying energy-gap correlation function

$$\zeta_{pq}(t) = \langle \delta\omega_{p,0}(t)\, \delta\omega_{q,0}(0)\rangle_B = \rho_{qp}\sigma_{pp}\sigma_{qq} \exp\left(-\frac{|t|}{\tau_{pq}}\right) \quad (23)$$

where τ_{pq} is the auto- ($p = q$) or cross- ($p \neq q$) correlation time and $\rho_{pp} \equiv 1$. The cross-correlation functions ζ_{pq} correlates the time scale and amplitude of frequency fluctuations between transitions. For ζ_{pq}, the correlation coefficient reflects the zero-time amplitude and the cross-correlation time $\tau_{pq} \leq \tau_{pp}, \tau_{qq}$.

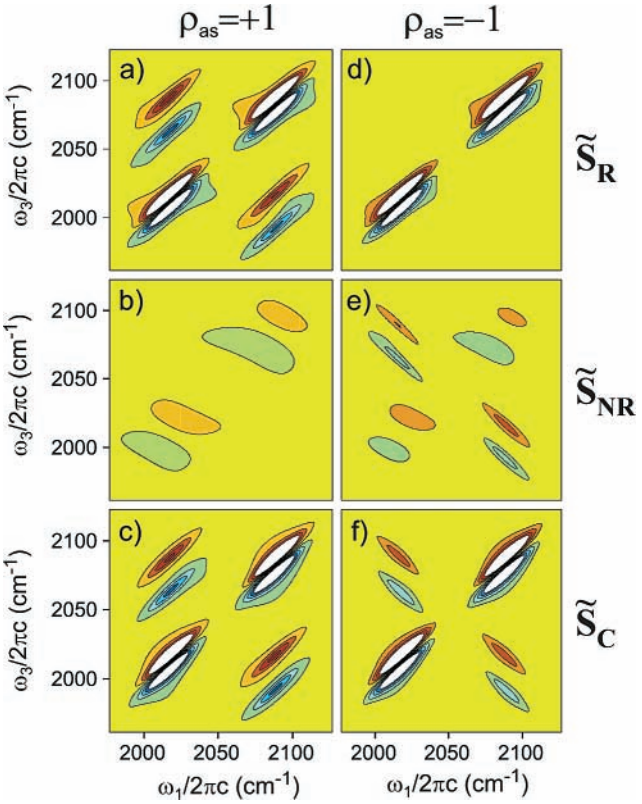

Figure 15. Effects of correlated line broadening on 2D line shapes for fully correlated ($\rho_{pq} = +1$) (a−c) and fully anticorrelated ($\rho_{pq} = -1$) (d−f) cases for rephasing (a, d), nonrephasing (b, e), and 2D correlation spectra (c, f). The simulations are done for the RDC six-level system assuming that the dynamics of system−bath interactions are completely separable into fast ($\Gamma_{aa} = \Gamma_{ss} = \Gamma_{as} = 2$ cm^{-1}) and slow ($\sigma_{aa} = \sigma_{ss} = \sigma_{as} = 10$ cm^{-1}) components. (Refer to the text and Supporting Information for more details.) Note that in the case of $\rho_{pq} = +1$ cross peaks are tilted parallel to the diagonal in the rephasing spectrum (a), and the amplitudes of the cross peaks are suppressed relative to diagonal peaks in the nonrephasing spectrum (b). For $\rho_{pq} = -1$, the cross peaks are tilted perpendicular to the diagonal, and their amplitudes are enhanced relative to the diagonal peaks in the nonrephasing spectrum (e) whereas the cross-peak amplitudes are suppressed in the rephasing spectrum (d). The difference in the cross-peak intensities in the correlation spectra (c−f) is due to the imbalance in the number of corresponding pathways in the generation of the nonrephasing signal. The contours are plotted at 8% intervals.

B. 2D IR Relaxation Experiments. The dynamics of these transition-energy fluctuations can be monitored, regardless of their origin, by 2D IR relaxation experiments, which involve collecting 2D IR correlation spectra as a function of the waiting time τ_2.[21,36] Changes in the 2D line shapes as a function of τ_2 are related to the magnitude and time scale of the fluctuations of a particular transition. For fluctuations characterized by a correlation time τ_c, the 2D line shapes will evolve from an inhomogeneous to a homogeneous shape as the waiting period is varied from $\tau_2 < \tau_c$ to $\tau_2 > \tau_c$. When the correlation time for the transition frequency fluctuations is longer than the time scale of the experiment ($\tau_1 + \tau_2 + \tau_3 \ll \tau_c$), we observe a 2D line shape in the inhomogeneous limit, $\sigma\tau_c \gg 1$ (Figure 13c). When $\tau_2 \gg \tau_c$, the system can sample all frequencies within the distribution on the time scale of the experiment, and the 2D line shapes will appear homogeneous (Figure 13a). For a single dynamical time scale, the change in line shape will represent the progression from elliptical to symmetric seen in Figure 13c−a. Because the cross-peak line shapes are influenced by the

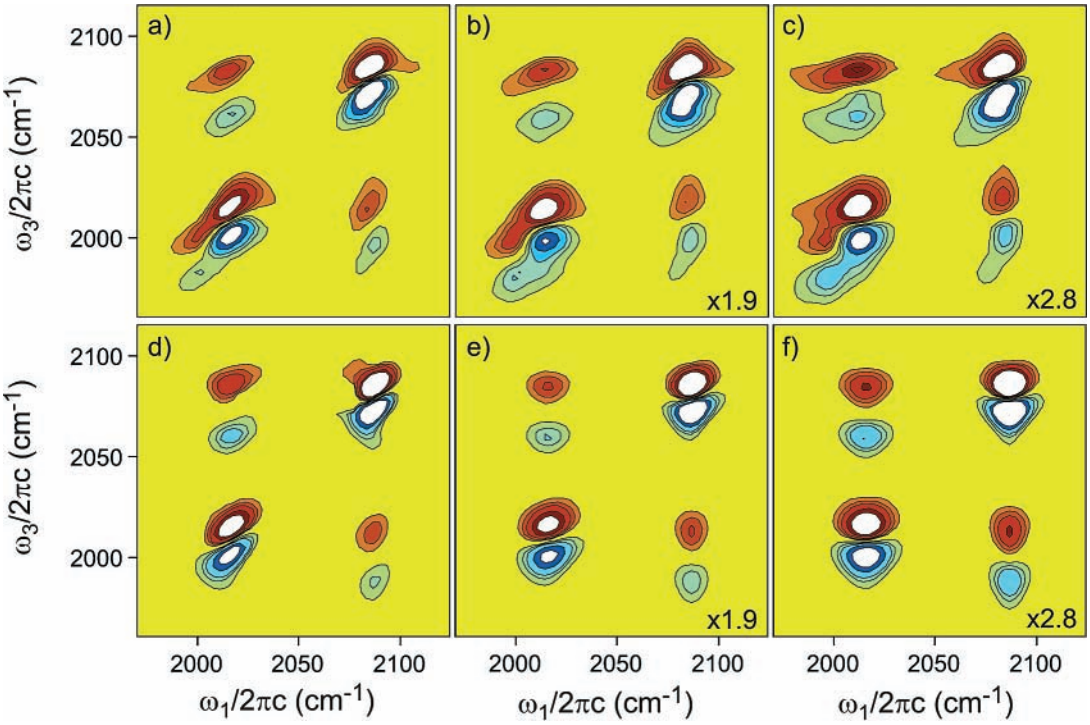

Figure 16. τ_2-dependent 2D IR correlation spectra of RDC in chloroform for τ_2 (a) 0, (b) 2.9, and (c) 6.2 ps and the corresponding spectra (d−f) calculated using the best-fit results with a correlation coefficient ρ_{as} of 0.9 ± 0.1. For other best-fit parameters, see the text. Note that for $\tau_2 = 0$ the diagonal peaks are elongated along the diagonal, showing the effects of inhomogeneous broadening. The cross peaks are also elongated and tilted parallel to the diagonal, indicating that the transition-energy fluctuations of coupled eigenstates *a* and *s* are fairly correlated as evident from $\rho_{as} = 0.9 \pm 0.1$. As τ_2 increases, the elongation becomes less pronounced, and the tilt disappears because of the exponential loss of memory of the initial frequencies. The observations indicate a system undergoing strongly correlated fluctuations on a picosecond time scale. Contour levels are 6% for the first three in each direction and 12% otherwise.

parameters describing the cross-correlation function ζ_{pq}, the time dependence of the rephasing (A_R) and nonrephasing amplitude (A_{NR}), and consequently that of Ψ, will be proportional to the dynamics of the correlated fluctuations.

Two-dimensional IR correlation spectra of RDC in chloroform were collected for waiting periods of $\tau_2 = 0$, 1.4, 2.9, 6.2, and 9.5 ps. Because Liouville pathways for cross peaks evolve as superpositions of the symmetric (s) and asymmetric (a) states during τ_2, these waiting times were chosen to correspond to the maxima of the quantum beats at $\omega^0_{s,a} = 71$ cm^{-1} (469 fs).[113,114] Figure 16 shows the 2D correlation spectra for $\tau_2 = 0$, 2.9, and 6.2 ps and illustrates the influence of the solvent on the frequency fluctuations of the coupled vibrations for RDC in $CHCl_3$. The four diagonal peaks are elongated along the diagonal, indicating a fairly inhomogeneous system. The cross peaks are also elongated and tilted parallel to the diagonal, which shows that the transition-energy fluctuations of eigenstates a and s are correlated ($\rho_{as} > 0$). For increased waiting times, the elongation of the line shapes becomes less pronounced, and the tilt disappears. Another signature of the time-dependent dynamics and the amplitude decay of the energy-gap correlation function during τ_2 is the apparent rotation of the node between positive and negative features from being aligned along the diagonal to being aligned along ω_3. This change arises from changes in the relative amplitudes of cross peaks in the rephasing and nonrephasing spectra ranging from a value of $A_R/A_{NR} \approx 6$ ($\Psi \approx 45°$) at $\tau_2 = 0$ to a value of ~1.2 ($\Psi \approx 15°$) at $\tau_2 = 9.5$ ps.[35] In a similar fashion, the difference between the magnitudes of two-color three-pulse photon echo peak shifts obtained from rephasing and nonrephasing experiments has been used to study solvation dynamics of coupled electronic transitions.[115] These features indicate solvent-induced frequency fluctuations that lead to a gradual loss of memory of the initial frequencies and their correlation, consistent with a system undergoing strongly correlated fluctuations on a picosecond time scale.

We used the correlation functions given in eq 23 to model the correlated solvation dynamics of the coupled vibrations of RDC. Omitting the harmonically forbidden transitions, there are 10 energy-gap correlation functions characterizing the dephasing dynamics of the system, which include a total of 20 amplitude and correlation-time parameters. However, this number is greatly reduced when the seven energy-gap correlation functions that involve doubly excited states are expressed using the two autocorrelation functions and a single cross-correlation function, ζ_{aa}, ζ_{ss}, or ζ_{as}. This results in eight independent parameters characterizing the system−bath dynamics. These include the correlation coefficient ρ_{as}, the energy-gap fluctuation amplitudes σ_{aa} and σ_{ss}, the fluctuations correlation times τ_{aa}, τ_{ss}, and τ_{as}, and the transition dipole strengths $\mu^{a,0}$ and $\mu^{s,0}$.

We calculated the total nonlinear response for rephasing, S_I, and nonrephasing, S_{II} (and S_{III} is included for $\tau_2 = 0$ only) experiments separately as a function of τ_1, τ_2, and τ_3 by evaluating the nonlinear dephasing functions for all of the Liouville pathways in the RDC six-level system and summing over all of the individual contribution for a given wavevector matching condition. The harmonic approximation for the correlation functions reduces the number of nonlinear dephasing functions required from 40 to 12, as described in the Supporting Information.[73] We also incorporated the effect of molecular reorientation on the dynamics for each time period τ_1, τ_2, and τ_3. The global nonlinear least-squares fitting of the 2D correlation spectra for all values of τ_2 uses a modified Levenberg−Marquart algorithm and a finite difference Jacobian. The best-fit parameters are $\mu^{a,0}/\mu^{s,0} = 1.06 \pm 0.04$, $\sigma_{aa} = 7.4 \pm 0.6$ cm^{-1}, $\sigma_{ss} = 5.2 \pm 0.4$ cm^{-1}, $\tau_{aa} = 2.0 \pm 0.2$ ps, $\tau_{ss} = 2.0 \pm 0.4$ ps, $\tau_{as} = 1.2 \pm 0.4$ ps, and $\rho_{as} = 0.9 \pm 0.1$, indicating a high degree

of correlation in the fluctuations of the two transitions. Figure 16d−f shows the 2D correlation spectra calculated using the best-fit parameters, which successfully reproduce the experimental spectra as a function of τ_2 in terms of the tilt of the cross and diagonal peaks, their degree of elongation, absorption line widths, and the intensities. A clear point of comparison is the apparent rotation of the node between positive and negative lobes.

From the elongation of the diagonal peaks in Figure 16, we can see that that the system is inhomogeneously broadened. This observation is consistent with the best-fit results, which give a $\sigma\tau_c$ product of 2.5 for the autocorrelation functions, proving that the dynamics are in the slow-modulation limit. Relative to the homogeneous 2D line shapes observed for RDC in hexane, RDC exhibits a considerable asymmetric broadening of the linear absorption line widths from 2.6 cm^{-1} in hexane to >8 cm^{-1} in chloroform (Figure 8), indicating that the disorder arises from the specific RDC−$CHCl_3$ interactions. It has been shown that fundamental and overtone frequencies of −C═O stretching vibrations of ketones exhibit large asymmetric broadening of the absorption band as well when dissolved in weakly H-bonding solvents such as CH_2Cl_2 and $CHCl_3$, with $CHCl_3$ having the larger effect.[116] RDC in CH_3OH solution also shows extensive broadening of the symmetric and asymmetric −C≡O absorption bands together with the red shifting of the −C═O stretching frequencies of the acetylacetonato ligand by ∼25 cm^{-1}.

A second set of diagonal and cross peaks shifted relative to the primary resonances may also arise from these weak H-bonding interactions. These resonances are seen along the diagonal at $(\omega_1, \omega_3) = (1998, 1998)$ cm^{-1}, below the diagonal at $(\omega_1, \omega_3) = (1998, 1980)$ cm^{-1} and along the off-diagonal at $(\omega_1, \omega_3) = (2076, 1980)$ cm^{-1} in the 2D correlation spectra of RDC. The existence of a second distinct species is very clear, and the corresponding additional resonances become more pronounced in 2D correlation spectra for $\tau_2 = 3$ and 6 ps as the diagonal elongation and the tilt of the cross peaks disappear. The τ_2 dependence of the 2D correlation spectra also indicates that the second species has a longer population lifetime and that the interconversion between two different species does not occur on our experimental time scale. These additional resonances, which are red shifted by ∼16 cm^{-1} from $\omega_{a,0}{}^0$, are relatively low-amplitude. From absorption spectra after exposure to ultraviolet light and using RDC recrystallized from different solvents, we can rule out impurities, photochemical products, and isotopomers of RDC as the origin of these new resonances. These observations suggest that there are two distinctly different solvated species, and the resulting 2D spectrum is a superposition of two different spectra, each of which has multiple 2D resonances. The effect of this relatively strong solvation for a second species is to shift the asymmetric vibration more than the symmetric. It is possible that these two species are RDC with $CHCl_3$ H-bonded to the −C═O of the acac ring and RDC with no H-bonding. This interaction would affect the asymmetric vibration to a greater extent because the H-bonding coordinate would be parallel to the asymmetric stretching coordinates. Although it has been shown for the iridium analogue of RDC that metal−metal interactions lead to dimer formation and associated extra resonances due to the change in molecular symmetry in C_6H_6 solution,[117] our experiments are performed at RDC concentrations too low to induce dimerization. An analogous feature suggesting that specific RDC−solvent interactions may induce a new resonance was seen for symmetric vibration in the FTIR spectrum of RDC in a polymer matrix at 150 K.[29]

The highly correlated fluctuations that were observed are consistent with solvent-induced frequency shifts to two strongly coupled vibrations. The metal−carbonyl stretching frequencies are very sensitive to the electron density of the metal atom because of $d_\pi-\pi^*$ bonding interactions that couple the vibrations in this system.[96] Because RDC is a planar (d^8) coordination compound, the Rh atom is exposed to solvent molecules in the primary solvation shell along the two axial coordinates. The fluctuations of the solvent density will modulate the electron density of the Rh atom through dispersive electrostatic interactions and change the vibrational potentials of the oscillators in a correlated manner. Another mechanism that would modulate the electron density of the Rh and cause correlated fluctuations of −C≡O stretching frequencies is the solvent-induced change in electron density of the π system of the acac ring, which interacts with the Rh nonbonding d orbital.[117] Additional modeling in the basis of a local C≡O mode Hamiltonian has also shown that the asymmetric linear absorption line shapes can be explained in terms of disorder in the individual local-mode anharmonicities, which would reflect the variation of the local solvent environment.[29,35,107]

X. Discussion and Outlook

The experiments described above were motivated by the need for methods capable of interrogating transient molecular structure in solution, describing structural variation, and following the dynamics of those structures. In a general sense, 2D IR spectra can be used to characterize time-dependent couplings both between vibrational coordinates and between vibrations and their surroundings. These quantities are necessary to describe the dynamics of molecules in solution. We have presented an approach for acquiring 2D IR correlation spectra and interpreting the underlying molecular dynamics through an analysis of the time-evolving positions, amplitudes, and line shapes of resonances in a 2D IR correlation spectrum. Even for a system as simple as the terminal carbonyl stretches of RDC, 2D IR experiments provide information that cannot be accessed by other methods and reveal a far more detailed and accurate picture of the solute structure, solute−solvent interactions, and vibrational relaxation dynamics than those obtained from other linear and nonlinear spectroscopies.

Information on the interactions between coordinates, their relative orientation, and their dynamics is revealed through analyses of cross peaks. For systems where the anharmonicities are comparable to the absorption line widths or systems with many overlapping resonances and/or structural heterogeneity, it may not be possible to isolate the cross peak from other spectral features with the current methods. Such cases necessitate the development of new, generalized ways to access different spectral features selectively in a 2D correlation spectrum. For example, linear combinations of 2D IR spectra of proteins and peptides taken with different polarization geometries have been shown to suppress contributions from the diagonal peaks and expose the underlying weaker cross peaks.[81,82] Additional selectivity may be achieved by manipulating the shape, phase, and timing of the input pulses, thereby changing the relative phase between the signal and local oscillator fields in rephasing and nonrephasing experiments. Methods analogous to phase cycling in multidimensional NMR could be used to isolate signal contributions and could eliminate the need to phase the 2D spectra in an ad hoc manner in the ω_1 dimension. Selectivity can also be achieved from multiresonant experiments that probe different types of vibrational species and further development in IR analogues of pulsed NMR experiments based on higher-order nonlinear spectroscopy.[118]

The Fourier transform (FT) method presented here using short, broadband pulses is often contrasted with the double-resonance (DR) pump−probe technique where the change in transmission of a broadband probe beam through a sample is monitored as a function of a tunable narrow-band pump pulse.[7,37] There are two fundamental differences in the experiments: (1) the DR method has an intrinsic local oscillator for heterodyne detection, and (2) the signal in the FT experiment includes contributions from interaction processes involving four different transition dipole moments, which are not present in the DR method. Because the transmitted probe acts as the local oscillator for intrinsic heterodyne detection, the DR experiment measures a correlation spectrum with rephasing and nonrephasing processes directly and avoids the complications of "phasing" 2D correlation spectra. However, without control of the local oscillator phase, the DR experiment will always measure an absorptive response, and there are advantages to analyzing rephasing and nonrephasing spectra separately. For instance, nonrephasing spectra can potentially reveal multiple overlapping transitions along the diagonal that would be merged together in rephasing or correlation spectra. The four-transition processes in FT experiments carry extra information about the sign of the transition dipole moments[2,119] and probe coherent dynamics of the coupled singly excited states during τ_2. The lack of these processes in DR experiments results in all Liouville pathways being dependent on one angle in the microscopic frame and the absence of peak 5 (see Figure 10c). Superpositions of singly excited vibrational levels are created during τ_2 in FT experiments, which modulate the amplitude of the cross peaks in rephasing spectra and diagonal peaks in nonrephasing spectra during the waiting period. Such dynamics can interfere with the modeling of structures that are derived from amplitudes in the spectrum. Finally, it should be noted that the DR methods are faced with an intrinsic tradeoff between time and frequency resolution in the choice of bandwidth for the pump field, a compromise that is not present in FT experiments. This becomes problematic for the study of systems where there is no intrinsic separation of time scales in the vibrational dynamics that could be used to choose an appropriate pump pulse length or bandwidth.

Referring to the flowchart in Figure 1, there are additions and modifications to consider when studying more complicated molecular systems. Besides the need to treat multiple vibrations, a proper treatment of nonlinear vibrational spectroscopy should account for vibrational dephasing, population relaxation dynamics, and reorientational dynamics, which occur on similar time scales. Here, only the effects of vibrational dephasing were included in the formulation of the system−bath interactions, and population relaxation was added phenomenologically. In multilevel systems, the fastest relaxation processes may indeed arise from population relaxation. Methods are required to account for coherent and incoherent population transfer processes to describe the positions, amplitudes, and line widths of the resonances in 2D IR spectra accurately.[34,120] Ongoing studies of 2D IR spectra of RDC in hexane collected as a function of the waiting period provide clear evidence of coherence transfer and incoherent population transfer among the two-coupled symmetric and asymmetric eigenstates. These relaxation processes affect the determination of angles between the two-coupled vibrations and substantiate the claim that the determination of structural variables cannot be decoupled from the treatment of bath-induced relaxation processes. Also, steps should be taken toward modeling the 2D IR spectrum in the local-mode basis. Our approach to integrating the structure of the system with the bath-induced dynamics starts with a local-mode description of the system states and introduces the system−bath interactions at the level of the system eigenstates. Although this approach has certain advantages at the level of theory, insight into the specific structural changes induced by the bath maybe lost. In general, one would like to incorporate the effects of the system−bath interactions in the local-mode picture, allowing a direct modeling of time-dependent conformational fluctuations in solution. The nonlinear exciton equations presented by Mukamel and co-workers have been developed with this in mind.[1]

The observations presented here suggest that 2D IR methods will find broad application in the study of chemical, physical, and biological problems. For the study of liquids and solutions, a tool that reveals intra- and intermolecular interactions forms the basis for understanding the types of forces that govern liquid structure, conformational changes, reaction dynamics, and transport processes. For studies of conformational changes or fluctuations, the correlated shifts between multiple vibrational transitions determined from 2D spectra can be used to deduce the amplitude and time scale of dynamics such as torsion angle motion. Correlated frequency shifts induced by variation of coupling and/or interaction with a bath are often encountered in the study of disorder in excitons, particularly in molecular aggregates. Separation of the diagonal and off-diagonal disorder in such systems is a general problem that could be facilitated by 2D cross-peak line-shape analysis. Two-dimensional IR line-shape analysis and relaxation experiments on vibrational resonances that are particularly sensitive to local solvent structure, such as OH and NH resonances, can be used to reveal the many-body molecular dynamics of liquids and the structural details of solvation. For such experiments, computational methods including molecular dynamics simulation and ab initio methods will be important in helping to correlate intermolecular structure with vibrational frequency shifts.[40,41,121−123] In molecular liquids, these techniques also promise to help address questions about heterogeneous dynamics, in which the dynamics of different subensembles vary. To the degree that these subensembles can be separated by frequency and the time scale of dynamics, the 2D IR line shape can also be used to characterize the degree of heterogeneity and the time scale of interchange between ensembles. The applicability of these methods extends well beyond liquids and solution-phase problems. Numerous other condensed matter systems including molecular crystals, semiconductors, quantum dots, and interfaces could draw on 2D techniques either in the optical, infrared, or terahertz regimes to study the interactions of electrons, nuclei, and/or collective coordinates such as phonons. Also, in the gas phase, 2D methods stand to help considerably with revealing couplings and orientation and assigning progressions in congested spectra.

One of the most appealing consequences of a transient structural tool is that 2D IR spectroscopy can be used as a probe of nonequilibrium processes such as optically initiated chemical reactions or biophysical processes. Photochemical triggering of a chemical reaction can be followed with 2D IR probing to deduce the structural changes accompanying the event. Alternatively, one can imagine correlating the structure of reactants and products in such a process by phototriggering during the waiting period. Two-dimensional IR could also be coupled with a variety of rapid initiation techniques that exist for biophysical processes such as protein folding, denaturing, or binding of a substrate.

Realizing these applications still requires advances in the experimental procedures and the extension of theoretical models

and data analysis tools. This further development promises to increase the applicability of 2D IR spectroscopy as a commonly used analytical tool to study systems with many degrees of freedom. Through its ability to reveal structural information on a disordered ensemble with picosecond time resolution, new insight will be obtained into intra- and intermolecular forces in condensed phases, which in turn will help in the development of models and theoretical tools for studying highly complex systems. By using 2D IR methods to follow structural changes during time-dependent chemical processes either near equilibrium with relaxation experiments or probing after the rapid optical initiation, we can hope to observe chemical dynamics in solution directly.

Acknowledgment. We thank Dr. Jaeyoung Sung for many conversations regarding the nonlinear response for a multilevel vibrational system. This work was supported by the National Science Foundation through a grant to A.T. (CHE-0079268) and the Laser Research Facility at MIT (CHE-0111370), Basic Energy Sciences of the U.S. Department of Energy (DE-FG02-99ER14988), and the donors of the ACS-Petroleum Research Fund. A.T. thanks the David and Lucile Packard Foundation for a fellowship.

Supporting Information Available: Details necessary to calculate 2D IR correlation spectra of multilevel systems using our model compound as an example are available, including (1) expressions for the nonlinear dephasing functions in the homogeneous and inhomogeneous limit and the harmonic approximation used to reduce the number of unique dephasing functions in a multilevel system, (2) a calculation of the nonlinear orientational response for symmetric diffusers along with the nonvanishing tensor components of a spherical diffuser containing two orthogonal dipoles, and (3) a detailed listing of all of the parameters used to calculate the 2D IR spectrum of RDC, which includes Feynman diagrams for all the Liouville-space pathways, explicit expressions for the orientational factors, and best fit eigenstate and local mode parameters resulting from the fitting of the 2D IR spectra of RDC in hexane. This material is available free of charge via the Internet at http://pubs.acs.org.

References and Notes

(1) Mukamel, S. *Annu. Rev. Phys. Chem.* **2000**, *51*, 691.
(2) Jonas, D. M. *Annu. Rev. Phys. Chem.* **2003**, *54*, 425.
(3) Ernst, R. R.; Bodenhausen, G.; Wokaun, A. *Principles of Nuclear Magnetic Resonance in One and Two Dimensions*; Oxford University Press: Oxford, U.K., 1987.
(4) Aue, W. P.; Bartholdi, E.; Ernst, R. R. *J. Chem. Phys.* **1976**, *64*, 2229.
(5) Ge, N.-H.; Hochstrasser, R. M. *PhysChemComm* **2002**, *3*, 1.
(6) Zanni, M. T.; Hochstrasser, R. M. *Curr. Opin. Struct. Biol.* **2001**, *11*, 516.
(7) Woutersen, S.; Hamm, P. *J. Phys.: Condens. Matter* **2002**, *14*, R1035.
(8) Mukamel, S.; Piryatinski, A.; Chernyak, V. *Acc. Chem. Res.* **1999**, *32*, 145.
(9) Cho, M. *PhysChemComm* **2002**, *7*, 1.
(10) Cho, M. Two-Dimensional Vibrational Spectroscopy. In *Advances in Multi-Photon Processes and Spectroscopy*; Fujimura, Y., Lin, S. H., Eds.; World Scientific: Singapore, 1999; Vol. 12, p 229.
(11) Blank, D.; Fleming, G. R.; Cho, M.; Tokmakoff, A. In *Ultrafast Infrared and Raman Spectroscopy*; Fayer, M. D., Ed.; Marcel Dekker: New York, 2001; p 437.
(12) Fourkas, J. T. *Annu. Rev. Phys. Chem.* **2002**, *53*, 17.
(13) Tominaga, K.; Maekawa, H. *Bull. Chem. Soc. Jpn.* **2001**, *74*, 279.
(14) Belabas, N.; Joffre, M. *Opt. Lett.* **2002**, *27*, 2043.
(15) Underwood, D. F.; Blank, D. A. *J. Phys. Chem. A* **2003**, *107*, 956.
(16) Tanimura, Y.; Mukamel, S. *J. Chem. Phys.* **1993**, *99*, 9496.
(17) Kubarych, K. J.; Milne, C. J.; Lin, S.; Astinov, V.; Miller, R. J. D. *J. Chem. Phys.* **2002**, *116*, 2016.
(18) Kaufman, L. J.; Heo, J.; Zieglar, L. D.; Fleming, G. R. *Phys. Rev. Lett.* **2002**, *88*, 2074021.
(19) Gallagher, S. M.; Albrecht, A. W.; Hybl, J. D.; Landin, B. L.; Rajaram, B.; Jonas, D. M. *J. Opt. Soc. Am. B* **1998**, *15*, 2338.
(20) Hybl, J. D.; Albrecht, A. W.; Gallager-Faeder, S. M.; Jonas, D. M. *Chem. Phys. Lett.* **1998**, *297*, 307.
(21) Hybl, J. D.; Ferro, A. A.; Jonas, D. M. *J. Chem. Phys.* **2001**, *115*, 6606.
(22) Hybl, J. D.; Yu, A.; Farrow, D. A.; Jonas, D. M. *J. Phys. Chem. A* **2002**, *106*, 7651.
(23) Zhao, W.; Wright, J. C. *Phys. Rev. Lett.* **2000**, *84*, 1411.
(24) Zhao, W.; Wright, J. C. *J. Am. Chem. Soc.* **1999**, *121*, 10994.
(25) Deak, J. C.; Rhea, S. T.; Iwaki, L. K.; Dlott, D. D. *J. Phys. Chem. A* **2000**, *104*, 4866.
(26) Dlott, D. D. *Chem. Phys.* **2001**, *266*, 149.
(27) Rector, K. D.; Fayer, M. D. *Int. Rev. Phys. Chem.* **1998**, *17*, 261.
(28) Merchant, K. A.; Thompson, D. E.; Fayer, M. D. *Phys. Rev. Lett.* **2001**, *86*, 3899.
(29) Thompson, D. E.; Merchant, K. A.; Fayer, M. D. *J. Chem. Phys.* **2001**, *115*, 317.
(30) Hamm, P.; Lim, M.; DeGrado, W. F.; Hochstrasser, R. *J. Phys. Chem. A* **1999**, *103*, 10049.
(31) Asplund, M. C.; Zanni, M. T.; Hochstrasser, R. M. *Proc. Natl. Acad. Sci. U.S.A.* **2000**, *97*, 8219.
(32) Khalil, M.; Demirdöven, N.; Tokmakoff, A. *Phys. Rev. Lett.* **2003**, *90*, 47401.
(33) Gallagher Faeder, S. M.; Jonas, D. M. *J. Phys. Chem. A* **1999**, *103*, 10489.
(34) Piryatinski, A.; Chernyak, V.; Mukamel, S. *Chem. Phys.* **2001**, *266*, 285.
(35) Demirdöven, N.; Khalil, M.; Tokmakoff, A. *Phys. Rev. Lett.* **2002**, *89*, 237401.
(36) Woutersen, S.; Mu, Y.; Stock, G.; Hamm, P. *Proc. Natl. Acad. Sci.* **2001**, *98*, 11254.
(37) Hamm, P.; Lim, M.; Hochstrasser, R. M. *J. Phys. Chem. B* **1998**, *102*, 6123.
(38) Piryatinski, A.; Tretiak, S.; Chernyak, V.; Mukamel, S. *J. Raman Spectrosc.* **2000**, *31*, 125.
(39) Piryatinski, A.; Chernyak, V.; Mukamel, S. In *Ultrafast Infrared and Raman Spectroscopy*; Fayer, M. D., Ed.; Marcel Dekker: New York, 2001.
(40) Scheurer, C.; Piryatinski, A.; Mukamel, S. *J. Am. Chem. Soc.* **2001**, *123*, 3114.
(41) Gnanakaran, S.; Hochstrasser, R. M. *J. Am. Chem. Soc.* **2001**, *123*, 12886.
(42) Okumura, K.; Tokmakoff, A.; Tanimura, Y. *Chem. Phys. Lett.* **1999**, *314*, 488.
(43) Tokmakoff, A. *J. Phys. Chem. A* **2000**, *104*, 4247.
(44) Yan, Y. J.; Mukamel, S. *J. Chem. Phys.* **1991**, *94*, 179.
(45) Joo, T.; Jia, Y.; Yu, J.-Y.; Lang, M. J.; Fleming, G. R. *J. Chem. Phys.* **1996**, *104*, 6089.
(46) Hybl, J. D.; Christophe, Y.; Jonas, D. M. *Chem. Phys.* **2001**, *266*, 295.
(47) Mukamel, S. *Phys. Rev. A* **1983**, *28*, 3480.
(48) Sung, J.; Silbey, R. J. *J. Chem. Phys.* **2001**, *115*, 9266.
(49) Sung, J.; Silbey, R. J. *J. Chem. Phys.* **2003**, *118*, 2443.
(50) Beckerle, J. D.; Casassa, M. P.; Cavanagh, R. R.; Heilweil, E. J.; Stephenson, J. C. *Chem. Phys.* **1992**, *160*, 487.
(51) Rector, K. D.; Fayer, M. D. *J. Chem. Phys.* **1998**, *108*, 1794.
(52) Golonzka, O.; Khalil, M.; Demirdöven, N.; Tokmakoff, A. *J. Chem. Phys.* **2001**, *115*, 10814.
(53) Golonzka, O.; Khalil, M.; Demirdöven, N.; Tokmakoff, A. *Phys. Rev. Lett.* **2001**, *86*, 2154.
(54) Khalil, M.; Tokmakoff, A. *Chem. Phys.* **2001**, *266*, 213.
(55) Cho, M. *Phys. Rev. A* **2000**, *61*, 023406.
(56) Cho, M. *J. Chem. Phys.* **2001**, *115*, 4424.
(57) Sung, J.; Cho, M. *J. Chem. Phys.* **2000**, *113*, 7072.
(58) Wilson, E. B.; Decius, J. C.; Cross, P. C. *Molecular Vibrations*; Dover Publications: New York, 1980.
(59) Child, M. S.; Lawton, R. T. *Faraday Discuss. Chem. Soc.* **1981**, *71*, 273.
(60) Mills, I. M.; Robiette, A. G. *Mol. Phys.* **1985**, *56*, 743.
(61) Mukamel, S. *Principles of Nonlinear Optical Spectroscopy*; Oxford University Press: New York, 1995.
(62) Herzberg, G. H. *Infrared and Raman Spectra of Polyatomic Molecules*; Krieger: Malabar, FL, 1991; Vol. 2.
(63) Steffen, T.; Fourkas, J. T.; Duppen, K. *J. Chem. Phys.* **1996**, *105*, 7364.
(64) Golonzka, O.; Tokmakoff, A. *J. Chem. Phys.* **2001**, *115*, 297.
(65) Hochstrasser, R. M. *Chem. Phys.* **2001**, *266*, 273.
(66) Lim, M.; Hochstrasser, R. M. *J. Chem. Phys.* **2001**, *115*, 7629.
(67) Cho, M.; Fleming, G. R.; Mukamel, S. *J. Chem. Phys.* **1993**, *98*, 5314.

(68) Butcher, P. N.; Cotter, D. *The Elements of Nonlinear Optics*; Cambridge University Press: Cambridge, U.K., 1990.
(69) Ge, N.-H.; Zanni, M. T.; Hochstrasser, R. M. *J. Phys. Chem. A* **2002**, *106*, 962.
(70) Heilweil, E. J.; Cavanaugh, R. R.; Stephenson, J. C. *J. Chem. Phys.* **1988**, *89*, 230.
(71) Arrivo, S. M.; Dougherty, T. P.; Grubbs, W. T.; Heilweil, E. J. *Chem. Phys. Lett.* **1995**, *235*, 247.
(72) Grubbs, W. T.; Dougherty, T. P.; Heilweil, E. J. *Chem. Phys. Lett.* **1994**, *227*, 480.
(73) Refer to the Supporting Information accompanying this paper.
(74) Tominaga, K.; Yoshihara, K. *Phys. Rev. Lett.* **1996**, *76*, 987.
(75) Tominaga, K.; Yoshihara, K. *Phys. Rev. A* **1996**, *55*, 831.
(76) Oxtoby, D. W. *Annu. Rev. Phys. Chem.* **1981**, *32*, 77.
(77) Steffen, T.; Duppen, K. *Chem. Phys.* **1998**, *233*, 267.
(78) Fourkas, J. T.; Kawashima, H.; Nelson, K. A. *J. Chem. Phys.* **1995**, *103*, 4393.
(79) Berne, B. J.; Pecora, R. *Dynamic Light Scattering*; R. E. Krieger Publishing Co.: Malabar, FL, 1990.
(80) Favro, L. D. *Phys. Rev.* **1960**, *119*, 53.
(81) Woutersen, S.; Hamm, P. *J. Phys. Chem. B* **2000**, *104*, 11316.
(82) Zanni, M.; Ge, N.-H.; Kim, Y. S.; Hochstrasser, R. M. *Proc. Natl. Acad. Sci. U.S.A.* **2001**, *98*, 11265.
(83) Scheurer, C.; Mukamel, S. *J. Chem. Phys.* **2001**, *115*, 4989.
(84) Krueger, B. P.; Scholes, G. D.; Fleming, G. R. *J. Phys. Chem. B* **1998**, *102*, 9603.
(85) Bachmann, P.; Aue, W. P.; Müller, L.; Ernst, R. R. *J. Magn. Reson.* **1977**, *28*, 29.
(86) States, D. J.; Haberkorn, R. A.; Ruben, D. J. *J. Magn. Reson.* **1982**, *48*, 286.
(87) Keusters, D.; Tan, H.-S.; Warren, W. S. *J. Phys. Chem. A* **1999**, *103*, 10369.
(88) Hybl, J. D.; Gallagher Faeder, S. M.; Albrecht, A. W.; Tolbert, C. A.; Green, D. C.; Jonas, D. M. *J. Lumin.* **2000**, *87*−*89*, 126.
(89) Derome, A. D. *Modern NMR Techniques for Chemistry Research*; Pergamon Press: Oxford, U.K., 1987.
(90) Demirdöven, N.; Khalil, M.; Golonzka, O.; Tokmakoff, A. *Opt. Lett.* **2002**, *27*, 433.
(91) Dorrer, C.; Belabas, N.; Likforman, J.-P.; Joffre, M. *J. Opt. Soc. Am. B* **2000**, *17*, 1795.
(92) Okumura, K.; Tanimura, Y. *J. Chem. Phys.* **1997**, *107*, 2267.
(93) Kubo, R. *Adv. Chem. Phys.* **1969**, *15*, 101.
(94) Cotton, F. A.; Wilkinson, G. *Advanced Inorganic Chemistry*, 5th ed.; Wiley & Sons: New York, 1988.
(95) Huq, F.; Skapski, A. C. *J. Cryst. Mol. Struct.* **1974**, *4*, 411.
(96) Huheey, J. E.; Keiter, E. A.; Keiter, R. L. *Inorganic Chemistry: Principles of Structure and Reactivity*, 4th ed.; HarperCollins College Publishers: New York, 1993.
(97) Krimm, S.; Bandekar, J. *Adv. Protein Chem.* **1986**, *38*, 181.
(98) Torii, H.; Tasumi, M. *J. Chem. Phys.* **1992**, *95*, 3379.
(99) Hamm, P.; Woutersen, S. *Bull. Chem. Soc. Jpn.* **2002**, *75*, 985.
(100) Cha, S.; Ham, S.; Cho, M. *J. Chem. Phys.* **2002**, *117*, 740.
(101) Friedrich, J.; Haarer, D. *J. Chem. Phys.* **1983**, *79*, 1612.
(102) Sevian, H. M.; Skinner, J. L. *Theor. Chim. Acta* **1992**, *82*, 29.
(103) Cundiff, S. T. *Phys. Rev. A* **1994**, *49*, 3114.
(104) Erland, J.; Pantke, K.-H.; Mizeikis, V.; Lyssenko, V. G.; Hvam, J. M. *Phys. Rev. B* **1994**, *50*, 15047.
(105) Venkatramani, R.; Mukamel, S. *J. Chem. Phys.* **2002**, *117*, 11089.
(106) Dick, B.; Hochstrasser, R. M. *J. Chem. Phys.* **1983**, *78*, 3398.
(107) Demirdöven, N.; Khalil, M.; Golonzka, O.; Tokmakoff, A. *J. Phys. Chem. A* **2001**, *105*, 8025.
(108) Knapp, E. W. *Chem. Phys.* **1984**, *85*, 73.
(109) Knoester, J. *J. Chem. Phys.* **1993**, *99*.
(110) Yang, M.; Fleming, G. R. *J. Chem. Phys.* **2000**, *113*, 2823.
(111) Woutersen, S.; Hamm, P. *J. Chem. Phys.* **2001**, *115*, 7737.
(112) Bosma, W. B.; Yan, Y. J.; Mukamel, S. *Phys. Rev. A* **1990**, *42*, 6920.
(113) Schoenlein, R. W.; Mittleman, D. M.; Shiang, J. J.; Alivisatos, A. P.; Shank, C. V. *Phys. Rev. Lett.* **1993**, *70*, 1014.
(114) de Boeij, W. P.; Pshenichnikov, M. S.; Wiersma, D. A. *J. Chem. Phys.* **1996**, *105*, 2953.
(115) Agarwal, R.; Prall, B. S.; Rizvi, A. H.; Yang, M.; Fleming, G. R. *J. Chem. Phys.* **2002**, *116*, 6243.
(116) Sahini, V. E.; Olteneanu, M. *Rev. Roum. Chim.* **1972**, *18*, 361.
(117) Bonati, F.; Ugo, R. *J. Organomet. Chem.* **1967**, *11*, 341.
(118) Scheurer, C.; Mukamel, S. *J. Chem. Phys.* **2002**, *116*, 6803.
(119) Gallagher Faeder, S. M.; Jonas, D. M. *Phys. Rev. A.* **2000**, *62*, 033820.
(120) Bree, P. d.; Wiersma, D. A. *J. Chem. Phys.* **1979**, *70*, 790.
(121) Rey, R.; Moller, K. B.; Hynes, J. T. *J. Phys. Chem. A* **2002**, *106*, 11993.
(122) Lawrence, C. P.; Skinner, J. L. *J. Chem. Phys.* **2003**, *118*, 264.
(123) Mu, Y.; Stock, G. *J. Phys. Chem. B* **2002**, *106*, 5294.